Chemical Engineering Journal 481 (2024) 148611

Contents lists available at ScienceDirect

Chemical Engineering Journal

journal homepage: www.elsevier.com/locate/cej

Cancer cell membrane proteins-encapsulated nanovaccine enhances cancer immunotherapy and prevention by provoking antigen-specific cellular immunity via the dendritic cell-targeted delivery

Xingyu Luo [a,1], Xiaolu Chen [b,1], Rongying Ma [a], Zhaoming Fu [a], Zuwei Liu [a], Qianhong Su [a], Huiling Fu [a], Yong Yang [a,*], Wei Xue [c,*]

[a] Key Laboratory of Food Nutrition and Functional Food of Hainan Province, School of Food Science and Engineering, Hainan University, Haikou 570228, China
[b] Tropical Crops Genetic Resources Institute, Chinese Academy of Tropical Agricultural Science, Haikou 570100, China
[c] Key Laboratory of Biomaterials of Guangdong Higher Education Institutes, Guangdong Provincial Engineering and Technological Research Center for Drug Carrier Development, Department of Biomedical Engineering, Jinan University, Guangzhou 510632, China

ARTICLE INFO

Keywords:
Metal-phenolic networks
Cancer nanovaccine
Mannose receptor
Cytotoxic T cell
Cancer immunotherapy

ABSTRACT

Cancer nanovaccines offer a promising strategy for fighting against tumors, however, the engineering of cancer nanovaccines that can be easily fabricated with tanglesome cancer cell-derived antigens and elicit an adequately strong tumor-specific cellular immunity remains challenging. Herein, metal-phenolic networks (MPNs) are used as an antigen delivery platform to prepare the mannose-modified MPNs nanovaccine loaded with ovalbumin (OVA) and the immunoadjuvant CpG oligodeoxynucleotide (MMOC) through the facile self-assembly. When the model antigen OVA is substituted with cancer cell membrane proteins (CCMPs), the nanovaccine is called MMCC. MMOC markedly activates dendritic cells (DCs) via the mannose-mediated endocytosis and efficiently promotes the antigen cross-presentation, thus inspiring a robust antigen-specific $CD8^+$ T cell response as well as immune memory effect *in vivo*. Consequently, MMOC exhibits admirable therapeutic and preventive results on E.G7-OVA tumors. Moreover, the combination use of MMCC with anti-PD1 significantly inhibits the growth of 4T1 tumors by strengthening the cellular immunity and decreasing the proportion of regulatory T cells (Tregs). The survival rate of 4T1 tumor-bearing mice in the prophylaxis assay is maintained at 100 % by MMCC over 42 days. Altogether, this study affords a universal and effective nanovaccine preparation strategy for cancer immunotherapy and prevention.

1. Introduction

Over the past decade, cancer immunotherapy that uses the body's own immune system to fight against cancer cells has brought a tremendous new vitality to the development of cancer treatments. Among the different cancer immunotherapy schemes [1,2], such as immune checkpoint blockade (ICB), and chimeric antigen receptor T cell (CAR-T) immunotherapy, etc., the cancer vaccine therapy has been investigated based on theory and its clinical application [3]. Usually, cancer whole-cell antigens (CWCAs), directly derived from cancer cell lysates [4–6] or membranes [7,8], have been considered to be superior to cancer-associated antigens [9,10] and cancer-specific antigens [11,12], due to their ease of production, low cost, relative integrality of cancer cell antigens, and ability to enable a broad spectrum of antitumor immune responses [13]. Generally, CWCAs are used as the source of cancer vaccines, and assumed to inhibit the progression of pre-existing tumor and prevent the occurrence of tumors by eliciting a tumor-specific immune response [14].

Nevertheless, toward triggering the adequate antitumor cellular immunity, CWCAs have to follow a number of pathways: 1) CWCAs are captured and internalized by antigen presenting cells (APCs), especially dendritic cells (DCs) [15]; 2) CWCAs escape from lysosomes and undergo cross-presentation [16]; 3) Mature DCs home to lymph nodes and present antigen epitopes to T cells via the major histocompatibility complex class I (MHC I) pathway, subsequently stimulating the cytotoxic T cells (CTLs) [17]. However, as a matter of fact, free CWCAs often

* Corresponding authors.
E-mail addresses: yangyong@hainanu.edu.cn (Y. Yang), weixue_jnu@aliyun.com (W. Xue).
[1] These authors contributed equally to this work.

https://doi.org/10.1016/j.cej.2024.148611
Received 24 September 2023; Received in revised form 18 November 2023; Accepted 5 January 2024
Available online 6 January 2024

fail to achieve such an ideal immune regulating result, because they are inherently susceptible to degradation *in vivo*, and they may be inefficiently ingested by DCs. As exogenous antigens, CWCAs are also prone to evoke humoral immunity rather than cellular immunity [18–20]. Taking these into consideration, the induction of a notable CTLs-mediated antitumor immune effect, thus depends on the efficient delivery of CWCAs into DCs and the sufficient activation of DCs.

To address these issues, new developments in nanotechnology provide some exciting possibilities. The use of nanocarriers can bring many benefits for the antigen delivery, including efficient antigen-loading properties, protection of antigens from *in vivo* degradation, and a spatio-temporal controlled release profile [21,22]. Moreover, the surface of nanovaccines consisting of nanocarriers and antigens can be equipped with a targeting moiety through physical or chemical conjugation to achieve targeted delivery [23,24]. Particularly, it is well known that mannose receptors belonging to C-type lectin superfamily usually have a high expression on the membrane of DCs. When the surface of nanovaccine is modified with mannose molecules, nanovaccine can be efficiently ingested by DCs via the specific binding between mannose molecules and mannose receptors so as to remarkably increase the antigen utilization [25–28]. Upon being endocytosed, some functionalized nanovaccines can promote the escape of antigen from lysosomes via the proton sponge effect [29,30] or by structural transformation [31]. Consequently, exogenous antigens tend to be processed by the MHC I pathway during cross-presentation to provoke the $CD8^+$ T cell response. Moreover, toll-like receptor (TLR) 9 agonists, and CpG oligodeoxynucleotide (CpG), for instance, can stimulate the secretion of proinflammatory cytokines, leading to the helper T cell type 1 (Th1)-biased cellular immune response [32,33]. Hence, the codelivery of cancer antigen and immunostimulant into DCs can be implemented by nano-vehicles, which synergistically motivate marked antitumor immunity [34]. While many cancer nanovaccines based on CWCAs have been investigated, the tedious preparation, poor biosecurity, and low efficiency in the immune activation hinder their practical applications [35,36]. As a result, novel nanovaccines that can be rationally designed and easily constructed, and have a better biocompatibility are needed to improve the cancer vaccination strategy.

Metal-phenolic networks (MPNs) are an array of amorphous and

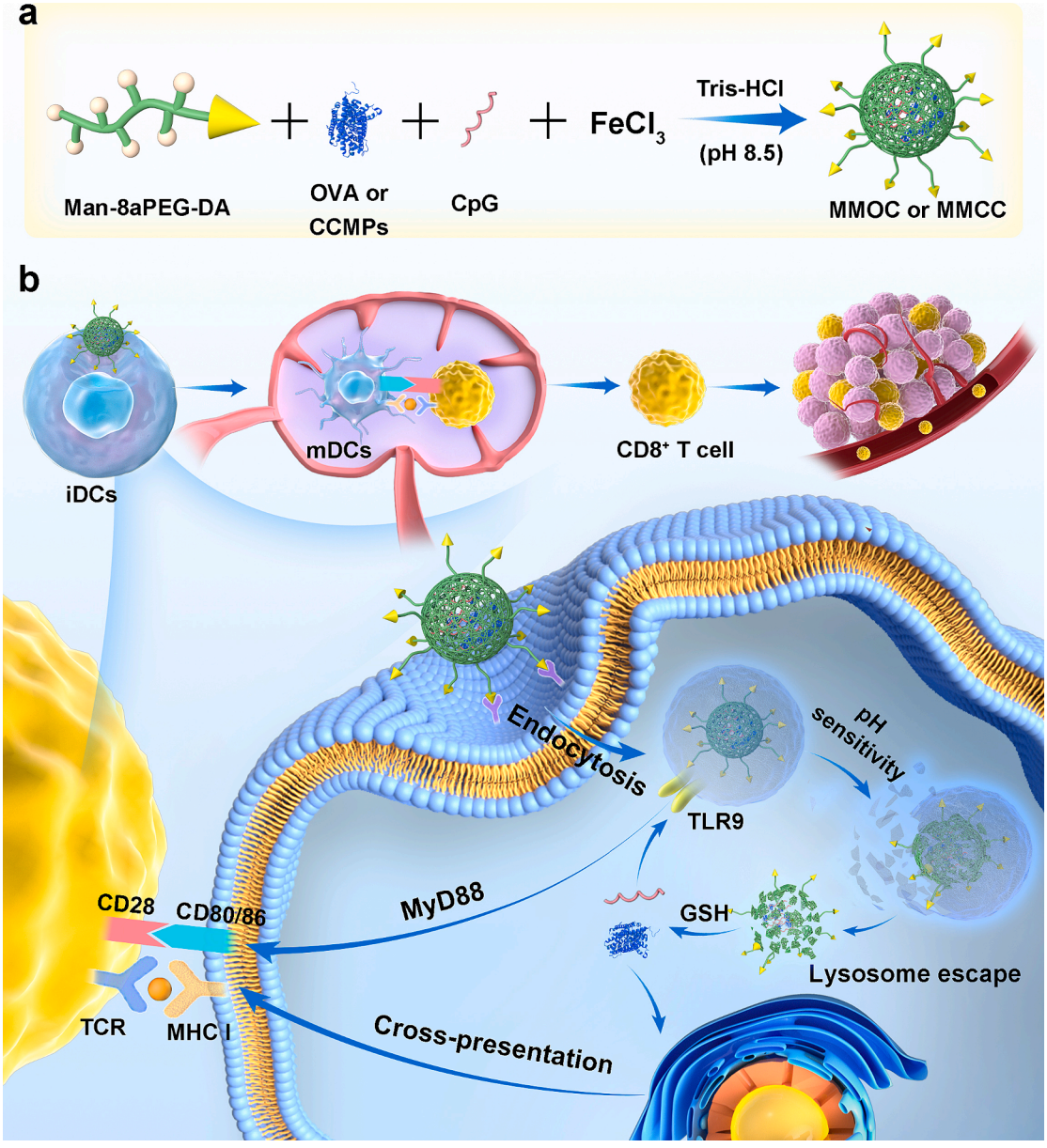

Scheme 1. Illustration for a) the preparation of MMOC and MMCC and b) the activation process of cellular immunity by the nanovaccine.

porous materials composed of polyphenol molecules and polyvalent metal ions [37,38]. By virtue of the simple coordination reaction between phenolic hydroxyl groups and metal ions, nano-sized MPNs can be easily and rapidly fabricated [39]. During the self-assembly of MPNs nanoparticles, multiple bioactive components can be concurrently loaded in order to produce a synergistic, multifarious action [40]. Additionally, because the composition of MPNs just contains natural or polyethylene glycol (PEG)-derived polyphenols and endogenously widespread metal ions (i.e., Fe^{3+} or Cu^{2+}), they usually exhibit good biosafety characteristics and are suitable for *in vivo* application [41]. Especially, dopamine (DA) molecules can be grafted at the tail ends of multi-arms PEG polymers, which makes multi-arms PEG have several catechol groups. As a result, the catechol group-terminated multi-arms PEG can be used as a polyphenol substance to prepare biocompatible MPNs. On account of these peculiarities, MPNs as nanocarriers have been widely explored for possible use in different cancer treatments, such as chemotherapy [42,43], immunotherapy [44,45], radiotherapy [46,47], photothermal therapy [48–50], and photodynamic therapy [51]. Nevertheless, the applications of MPNs in cancer vaccines are rarely seen [52], especially in the DCs-targeted delivery of CWCAs. Ultimately, an efficient MPNs-based cancer nanovaccine that can elicit a robust antitumor immune response is still worthy of a high expectation.

In this study, we fabricated cancer nanovaccines by employing MPNs nanoparticles as the antigen delivery vector. When the MPNs were quickly self-assembling, antigen and immunoadjuvant CpG were synchronously encapsulated into the nanoparticles whose surface has been successfully decorated with mannose. As shown in Scheme 1a, ovalbumin (OVA) and cancer cell membrane proteins (CCMPs) were severally used as the antigen to produce the mannose-modified MPNs nanovaccine loaded with OVA and CpG (called MMOC), and the mannose-modified MPNs nanovaccine loaded with CCMPs and CpG (called MMCC). MMOC and MMCC were readily recognized and engulfed by immature DCs (iDCs) through the interaction between mannose and mannose receptor. CpG and the antigen cross-presentation greatly excited DCs, and then mature DCs (mDCs) moved back to lymph nodes and enabled $CD8^+$ T cells via the MHC I pathway (Scheme 1b). MMOC was applied to *in vitro* and *in vivo* assays to investigate its ability to activate antigen-specific cellular immune responses and the efficacy on destroying and preventing E.G7-OVA tumors. Moreover, the effectiveness of MMCC to suppress 4T1 tumor progression and occurrence was further evaluated. This study highlights the potential of a novel antigen delivery platform based on MPNs to improve the cancer immunotherapy and prevention outcome.

2. Materials and methods

2.1. Materials

Eight arms PEG with N-hydroxysuccinimide esters (8aPEG, tripentaerythritol, Mw = 20,000) was purchased from JenKem Technology (Beijing, China), and single chain PEG with mannose and amino terminals (Man-PEG-NH_2, Mw = 2000) was obtained from Ponsure Biotechnology (Shanghai, China). Dopamine hydrochloride, triethylamine, $FeCl_3{\cdot}6H_2O$, tris(hydroxymethyl)aminomethane (Tris), and dimethyl formamide (DMF) were provided by Aladdin (Shanghai, China). Ovalbumin (OVA) was obtained from Sigma-Aldrich (Shanghai, China). CpG oligodeoxynucleotide (TCCATGACGTTCCTGACGTT) and CpG-Cy5 were ordered from Sangon Biotech (Shanghai, China). G418, β-mercaptoethanol, monensin, and brefeldin A were obtained from Yuanye Biotechnology (Shanghai, China). Recombinant murine GM-CSF and IL-4 were bought from PeproTech (USA). DNase I, hyaluronidase, and Bradford protein assay kit were purchased from Solarbio (Beijing, China). Hoechst 33258, DAPI, Lysotracker red, CCK-8 assay kit, and collagenase IV were purchased from Yeasen Biotechnology (Shanghai, China). Enhanced BCA protein assay kit, Triton X-100, and membrane and cytosol protein extraction kit were purchased from Beyotime (Shanghai, China). Anti-PD1 antibody was bought from BioXCell (USA). Mouse IL-6 (catalog no. 431304), IL-12p70 (catalog no. 433604), TNF-α (catalog no. 430904), and IFN-γ (catalog no. 430804) ELISA kits were obtained from Biolegend (USA). Anti-mouse MHC II-PE (catalog no. 12-5321-82), anti-mouse SIINFEKL-H-2Kb-PE (catalog no. 12-5743-82), anti-mouse CD11c-FITC (catalog no. 11-0114-82), anti-mouse CD80-PerCP-eFluor 710) (catalog no. 46-0801-82), and anti-mouse CD86-APC (catalog no. 17-0862-82) were bought from Invitrogen (USA). Anti-mouse Foxp3-PE (catalog no. 126404), anti-mouse CD8a-PE (catalog no. 100708), anti-mouse CD25-APC (catalog no. 102012), anti-mouse CD3-PerCP/Cy5.5 (catalog no. 100218), anti-mouse CD4-FITC (catalog no. 100406), anti-mouse IFN-γ-FITC (catalog no. 505806), Flex-T biotin H-2Kb OVA monomer (SIINFEKL) (catalog no. 280051), streptavidin-FITC (catalog no. 405201), anti-mouse CD62L-PerCP/Cy5.5 (catalog no. 104431), and anti-mouse CD44-APC (catalog no. 156003) were purchased from Biolegend (USA). Anti-mouse CD107a-FITC (catalog no. Ab24871) was obtained from Abcam (UK).

2.2. Cell culture and animals

DC2.4 (catalog no. CL-0545) and 4T1 (catalog no. CL-0007) cells were purchased from Procell Life Science&Technology Co., Ltd (Wuhan, China), and cultured with RPMI-1640 complete medium containing 10 % fetal bovine serum (FBS) and 1 % penicillin–streptomycin. E.G7-OVA cells (catalog no. CTCC-001–0136) were obtained from MeisenCTCC (Panan, China) and cultivated in RPMI-1640 medium containing G418 (0.4 mg/ml), β-mercaptoethanol (0.05 mM), 10 % FBS, and 1 % penicillin–streptomycin. All cells were maintained in a humidified incubator at 37 °C with 5 % CO_2.

Female BALB/c mice and C57BL/6 mice (6–8 weeks) were bought from Hunan SJA Laboratory Animal Co., Ltd (Changsha, China). Mice were housed in a room with constant temperature of 25 ± 2 °C, relative humidity of 40–70 %, and artificial light of 12 h dark-light cycle. All mice received attentive care with ad libitum access to food and water. All animal experiments were conducted according to the guidelines for the Care and Use of Laboratory Animals, and approved by the Ethics Committee of Hainan University (approval ID: HNUAUCC-2020-00132).

2.3. Characterization

The hydrodynamic particle size and surface zeta potential of samples were measured by a Zetasizer Nano ZSE instrument (Malvern, UK). ^1H NMR spectra were recorded using a nuclear magnetic resonance spectrometer (Advance 400, Bruker, Germany). Fourier transform infrared spectra (FT-IR) were obtained by a FT-IR spectrometer (Frontier, PerkinElmer, USA). The morphology of nanoparticles was observed by a transmission electron microscopy (TEM) (JEM-2100F, JEOL, Japan). Flow cytometry analysis was conducted by a flow cytometer (CytoFLEX, Beckman, USA). Fluorescent images of cells were taken by a confocal laser scanning microscope (CLSM) (TCS SP8, Leica, Germany). The absorbance of microplates was recorded by a photometric microplate reader (Synergy LX, BioTek, USA).

2.4. Synthesis of Man-8aPEG-DA and 8aPEG-DA polyphenols

To obtain 8 arms PEG modified with mannose and dopamine (Man-8aPEG-DA), 8aPEG (100 mg) and Man-PEG-NH_2 (15 mg) were dissolved in 5 mL of anhydrous DMF, and then stirred for 0.5 h under N_2 protection. Subsequently, dopamine hydrochloride (7.6 mg) and triethylamine (10 μL) were added, and the reaction was carried out for another 8 h at room temperature under N_2 protection. The mixture was collected and dialyzed against deoxygenated H_2O, which had been adjusted by HCl to pH 4.5, using a dialysis bag with molecular weight cut-off of 3500 Da. Finally, the resultant product was lyophilized to get Man-8aPEG-DA.

The synthesis procedure of 8aPEG-DA with dopamine at tail ends was as like as above, but Man-PEG-NH_2 was never used throughout.

2.5. Preparation of OVA-based nanovaccines

The synthesized 8aPEG-DA (20 μL, 50 mg/mL), OVA (500 μL, 0.8 mg/mL), and $FeCl_3{\cdot}6H_2O$ (300 μL, 3 mg/mL) were mixed together by fast vortex. Then, 200 μL of Tris-HCl buffer solution (0.2 M, pH 8.5) containing CpG (0.281 mg/mL) was added. After stirred for 30 min, the mixture was centrifuged (21,000 rpm, 25 min). The solid at the tube bottom was MPNs nanoparticle loaded with OVA and CpG, which was named MOC.

After Man-8aPEG-DA (20 μL, 50 mg/mL), OVA (500 μL, 0.8 mg/mL), and $FeCl_3{\cdot}6H_2O$ (300 μL, 3 mg/mL) were mixed up, 200 μL of Tris-HCl buffer solution (0.2 M, pH 8.5) containing CpG (0.198 mg/mL) was added. When the reaction was completed, mannose-decorated MPNs nanoparticles carrying OVA and CpG (MMOC) were obtained by centrifugation (21,000 rpm, 25 min).

The preparation of mannose-modified MPNs nanoparticles loaded with OVA, abbreviated to MMO, was similar with MMOC, except that CpG was not used at all.

At the end of preparation process of various nanovaccines, the supernatants were gathered to quantify uncombined OVA and CpG by using Bradford protein assay kit and fluorescence spectrophotometer, respectively.

2.6. Acquisition of cancer cell membrane proteins (CCMPs)

To get CCMPs, well-grown 4T1 cells were harvested and lysed by using an ultrasonic cell crusher. The mixture was centrifuged (7000 g, 10 min) and the precipitate was abandoned. Subsequently, the supernatant underwent centrifugation again (18,000 g, 30 min). CCMPs were extracted from the precipitate with a membrane and cytosol protein extraction kit. The quantity of CCMPs were measured by an enhanced BCA protein assay kit.

2.7. Preparation of CCMPs-based nanovaccines

The preparation methods of MPNs nanoparticles loaded with CCMPs and CpG (MCC), mannose-decorated MPNs nanoparticles loaded with CCMPs and CpG (MMCC), and mannose-decorated MPNs nanoparticles loaded with CCMPs (MMC) were similar to MOC, MMOC, and MMO, respectively. It was just that CCMPs replaced OVA as antigens.

2.8. In vitro OVA release behavior of MMOC

MMOC was ultrasonically dispersed in different buffer solutions, including PBS of pH 5.0, PBS of pH 5.0 with 10 mM glutathione, PBS of pH 7.4, and PBS of pH 7.4 with 10 mM glutathione, at the OVA concentration of 400 μg/mL, and then incubated at 37 °C with shaking in a water bath. At the scheduled time points (1, 2, 4, 8, 12, 16, 24, and 30 h), solutions were centrifugated (21,000 rpm, 25 min), and 100 μL of supernatants were fetched to quantify released OVA by a Bradford protein assay kit. The remaining samples were redispersed and incubated again.

2.9. In vitro cytotoxicity evaluation

DC2.4 cells were seeded into 96-well plates at a density of 7×10^3 cells/well and incubated with complete media for 24 h. Then complete media were discarded, and MOC, MMO, and MMOC, which had been dispersed in basic media at a series of concentrations (31.3, 62.5, 125, 250, and 500 μg/mL), were severally transferred to the relevant wells. After 24 h treatment, CCK-8 solutions were added and maintained for another 2 h. Finally, the absorbance at 450 nm was detected by a photometric microplate reader.

2.10. Hemolysis assay

Blood was collected from healthy BALB/c mice and put into anticoagulant tubes. Red blood cells were obtained by centrifugation (3000 rpm, 15 min). The isolated blood cells (20 μL) were mixed with PBS solution, ultrapure H_2O, and MMOC solutions with different concentrations (31.3, 62.5, 125, 250, and 500 μg/mL). After 4 h incubation at room temperature, samples were centrifuged (3000 rpm, 15 min). Absorbances of the supernatants at 542 nm were measured and used to calculate the hemolysis rate based on the following formula.

$$\text{Hemolysis rate } (\%) = [\text{OD (sample)} - \text{OD (PBS)}]/[\text{OD } (H_2O) - \text{OD (PBS)}]$$

2.11. Synthesis of OVA-FITC and OVA-Cy7

OVA (20 mg) was dissolved in 10 mL of sodium carbonate solution (25 mM, pH 9.8). Then, 0.4 mg of FITC dissolved in DMSO was added. The reaction was conducted at room temperature in the dark for 18 h. After dialyzed against ultrapure H_2O, the solution was lyophilized to get FITC-labelled OVA (OVA-FITC).

OVA (20 mg) dissolved in 20 mL of PBS (50 mM, pH 7.4) was mixed with Cy7-NHS (0.4 mg) dissolved in 200 μL of DMSO. After stirred at room temperature for 1 h, the mixture was purified with a disposable PD-10 column (Sephadex G-25). In the end, Cy7-marked OVA (OVA-Cy7) was obtained through lyophilization.

2.12. In vitro antigen uptake and intracellular co-localization

DC2.4 cells were seeded into 12-well plates at the density of 1×10^5 cells/well and cultured for 24 h. Subsequently, free OVA-FITC, MOC, MMO, and MMOC were added at the OVA-FITC concentration of 10 μg/mL. After treated for 4 h, cells were collected and processed with flow cytometry analysis.

DC2.4 cells were cultured in CLSM-specific dishes at a density of 2×10^5 cells per dish for 24 h. Then, OVA-FITC + CpG-Cy5, MOC, MMO, and MMOC were added to the corresponding dishes, according to that the applied concentrations of OVA-FITC and CpG-Cy5 were 20 μg/mL and 4 μg/mL, respectively. After 4 h incubation, cells were washed with PBS, fixed with 4 % paraformaldehyde solution, and stained with Hoechst 33258 (10 μg/mL). Finally, the intracellular co-localization of OVA-FITC and CpG-Cy5 was analyzed by CLSM.

2.13. In vitro antigen lysosome escape

DC2.4 cells were seeded in CLSM-specific dishes at a density of 2×10^5 cells per dish, and treated with OVA-FITC, MOC, MMO, and MMOC at an OVA-FITC concentration of 20 μg/mL for 6 h. After washed with PBS, cells were stained with Lysotracker red (75 nM) and Hoechst 33258 (10 μg/mL) in sequence, and then fixed with 4 % paraformaldehyde. Finally, samples were observed by CLSM.

2.14. In vitro BMDCs activation and antigen cross-presentation

Briefly, bone marrow-derived dendritic cells (BMDCs) were obtained from the tibias and femurs of 6-week-old C57BL/6 mice. The cells were fostered in RPMI-1640 medium supplemented with 10 % FBS, 1 % penicillin–streptomycin, GM-CSF (20 ng/mL), and IL-4 (10 ng/mL). After cultivation of 6 days, loosely adherent immature BMDCs were collected for further assays.

To evaluate the maturation of BMDCs, collected cells were seeded in 12-well plates at a density of 2×10^5 cells/well, and then incubated with OVA, MOC, MMO, and MMOC (20 μg/mL OVA) for 16 h. After processing, cells were stained with anti-CD11c-FITC, anti-CD86-APC, anti-CD80-PerCP-eFluor 710, and anti-MHC II-PE. Flow cytometry was performed to analyze the mature situation of DCs. The culture media during co-incubation of BMDCs with different vaccine formulations were collected to ascertain the concentrations of secreted IL-6, IL-12p70, TNF-α, and IFN-γ using ELISA detection kits.

To estimate the antigen cross-presentation efficiency, collected BMDCs were treated with OVA, MOC, MMO, and MMOC like above. After the treatment, cells were stained with anti-CD11c-FITC and anti-SIINFEKL-H-2Kb-PE, and subsequently analyzed by flow cytometry.

2.15. Antigen accumulation in lymph nodes

To quantitatively analyze the antigen arriving in lymph nodes, BALB/c mice were randomly divided into 3 groups (n = 3) and subcutaneously injected with OVA, MOC, and MMOC in the groin, respectively. OVA was labelled with FITC and its dosage was 30 μg per mouse. After 24 h, mice were sacrificed, and lymph nodes were collected and ground to obtain cell suspensions. The cell suspensions were treated by an ultrasonic cell disruptor, which was followed by centrifugation. Amount of OVA-FITC in the supernatant was determined with the FITC fluorescence signals detected by a multifunctional enzyme-linked immunosorbent assay (ELISA) reader (TECAN, Infinite 200 pro, Switzerland).

To investigate the visible distribution of OVA labelled with FITC and CpG labelled with Cy5 in lymph nodes, BALB/c mice were inguinally injected with OVA + CpG, MOC, MMO, and MMOC, respectively, at a dose of 50 μg OVA per mouse. After 24 h, mice were euthanized, and then inguinal lymph nodes were collected and fixed with 4 % paraformaldehyde. The samples were sliced up by using a cryostat microtome (Leica, Germany). After DAPI staining was carried out, the distribution of OVA and CpG was observed by an Olympus FV3000 confocal microscope.

For *in vivo* fluorescence imaging, OVA was labelled with Cy7. BALB/c mice were subcutaneously administered with free OVA, MOC, and MMOC at the tail base (50 μg OVA per mouse). At different time intervals (2, 8, 24, and 48 h), mice were observed and photographed by an IVIS Lumina XR animal imaging equipment (PerkinElmer, USA).

2.16. In vivo immune responses

C57BL/6 mice were randomly assigned into 5 groups (n = 4), including PBS, OVA, MOC, MMO, and MMOC. The mice were immunized with various vaccine formulations via subcutaneous injection in the inguinal region 3 times at 7-day intervals, according to the dosage of 30 μg OVA and 6 μg CpG per mouse. On day 21, the mice were sacrificed, and their inguinal lymph nodes and spleens were harvested to prepare single-cell suspensions for further analysis. Sera were collected to determine the levels of IL-6, IL-12p70, IFN-γ, and TNF-α using relevant ELISA detection kits.

For DCs activation analysis, the lymphocytes from lymph nodes were stained with anti-CD11c-FITC, anti-CD86-APC, anti-CD80-PerCP-eFluor 710, and anti-MHC II-PE antibodies. For cross-presentation analysis, the lymphocytes from lymph nodes were stained with anti-CD11c-FITC and anti-SIINFEKL-H-2Kb-PE.

For T cell activation analysis, harvested splenocytes were stained with anti-CD3-PerCP/Cy5.5, anti-CD4-FITC, and anti-CD8a-PE. To investigate the activation of OVA-specific $CD8^+$ T cells, splenocytes were incubated with Flex-T biotin H-2Kb OVA monomer (SIINFEKL), streptavidin-FITC, anti-CD3-PerCP/Cy5.5, and anti-CD8a-PE, according to the standard protocol.

For analyzing the CTLs response, splenocytes were cultured for 6 h in RPMI-1640 medium supplemented with OVA (30 μg/mL), monensin (2 nmol/mL), and brefeldin A (20 nmol/mL). Upon completion of the incubation, cells were divided into 2 parts. One part was stained with anti-CD3-PerCP/Cy5.5, anti-CD8a-PE, and anti-CD107a-FITC, while the other part was stained with anti-CD3-PerCP/Cy5.5, anti-CD8a-PE, and anti-IFN-γ-FITC.

To demonstrate the immune memory response, splenocytes were stained with anti-CD4-FITC, anti-CD8a-PE, anti-CD62L-PerCP/Cy5.5, and anti-CD44-APC.

Finally, after washed with PBS, various stained cell samples were measured by flow cytometry.

2.17. In vivo biological safety evaluation

C57BL/6 mice were randomly divided into 5 groups (n = 4) and immunized with various vaccine formulations (PBS, OVA, MOC, MMO, and MMOC) 3 times, according to the dosage of 30 μg OVA and 6 μg CpG per mouse. On day 21, mice were sacrificed, and main organs (heart, liver, spleen, lung, and kidney) and sera were collected. After organs were subjected to paraffin embedding, slicing, and H&E staining sequentially, the tissue morphostructure was investigated by an inverted microscope. In addition, collected sera were tested for biochemical indexes, including aspartate aminotransferase (AST), alanine transaminase (ALT), L-lactate dehydrogenase (LDH), blood urea nitrogen (BUN), creatinine (CREA), and uric acid (UA).

2.18. Therapeutic study of OVA-based nanovaccines on E.G7-OVA tumors

On day 0, C57BL/6 mice were randomly divided into 5 groups (n = 5) and inoculated with 5×10^5 E.G7-OVA cells per mouse on the right flanks. On days 7 and 14, mice were vaccinated with PBS, OVA, MOC, MMO, and MMOC according to 30 μg OVA and 6 μg CpG per mouse. Body weights and tumor sizes of mice were recorded every 2 days Tumor volume was calculated with the formula of $V = (L \times W^2)/2$ (V: tumor volume, L: tumor length, W: tumor width). On day 18, mice were sacrificed, and tumors were collected to be weighted and photographed. Immunofluorescence analysis was conducted after tumors were stained with Ki67, TUNEL, CD4, CD8, and Foxp3 markers.

2.19. Prophylactic study of OVA-based nanovaccines on E.G7-OVA tumors

C57BL/6 mice were randomly divided into 5 groups (n = 5), including PBS, OVA, MOC, MMO, and MMOC. On days -21, -14, and -7, mice were immunized with different vaccine formulations according to 30 μg OVA and 6 μg CpG per mouse. On day 0, each mouse was subcutaneously injected with 5×10^5 E.G7-OVA cells on the right flank. Body weight and tumor size of mouse were recorded every 2 days. Once the tumor volume reached to 1500 mm^3, the mouse was euthanized. On day 46, the assay ended and remaining mice were euthanized.

2.20. Therapeutic study of CCMPs-based nanovaccines on 4T1 tumors

BALB/c mice were randomly divided into 5 groups (n = 5), including PBS, CCMPs, MCC, MMC, MMCC, and MMCC + anti-PD1. On day 0, mice were inoculated with 1×10^6 4T1 cells/mouse on the right flanks. Immunizations with different vaccine formulations were carried out on days 5, 12, and 19, based on 30 μg CCMPs and 6 μg CpG per mouse. In the MMCC + anti-PD1 group, 30 μg of anti-PD1 antibody was intravenously injected into the tail vein of each mouse on days 6, 10, 13, and 17. Body weight and tumor size of mouse were recorded every 2 days. On day 22, mice were sacrificed, and spleens and tumors were collected and processed into single-cell suspensions for following immune analyses.

On one hand, immune responses in spleens were evaluated. For T cell activation analysis, splenocytes were stained with anti-CD3-PerCP/Cy5.5, anti-CD4-FITC, and anti-CD8a-PE. For regulatory T cells (Tregs) analysis, splenocytes were stained with anti-CD4-FITC, anti-CD25-APC, and anti-Foxp3-PE. For immune memory analysis, splenocytes were stained with anti-CD4-FITC, anti-CD8a-PE, anti-CD62L-PerCP/Cy5.5, and anti-CD44-APC. Finally, all stained cell samples were measured by flow cytometry.

On the other hand, tumor-infiltrating lymphocytes were investigated by flow cytometry. The tumor tissues were cut into pieces and incubated with DNase, collagenase IV, and hyaluronidase for 30 min. Then tissues were ground and filtered through a cell strainer (70 μm) to obtain single-

cell suspensions. To demonstrate the activation of DCs in tumors, cell suspensions were stained with anti-CD11c-FITC, anti-CD86-APC, and anti-CD80-PerCP-eFluor 710. For infiltrated T cell analysis, cells were stained with anti-CD3-PerCP/Cy5.5, anti-CD4-FITC, and anti-CD8a-PE. For regulatory T cells (Tregs) analysis, cells were stained with anti-CD4-FITC, anti-CD25-APC, and anti-Foxp3-PE.

2.21. Prophylactic study of CCMPs-based nanovaccines on 4T1 tumors

BALB/c mice were randomly divided into 5 groups (n = 5) and vaccinated with PBS, CCMPs, MCC, MMC, and MMCC on days -19, -12, and -5, respectively, according to 30 μg CCMPs and 6 μg CpG per mouse. On day 0, each mouse was inoculated with 1×10^6 4T1 cells on the right flank. Body weight and tumor size were recorded every 2 days. Mouse was euthanized when its tumor volume exceeded 1500 mm^3. On day 42, the assay was terminated and remaining mice were euthanized. Tumors in every group were collected and treated with Ki67, CD4, CD8, and Foxp3 stainings for the immunofluorescence analysis.

2.22. Statistical analysis

Data were expressed as the mean ± SD unless specifically indicated. Statistical analyses were performed by using one-way ANOVA when compared groups were more than two groups. The significance between two groups was analyzed by using Student's *t*-test. Significant differences were expressed as follows: *p < 0.05, **p < 0.01, ***p < 0.001, and ****p < 0.0001. When the p value was greater than 0.05, it was considered to be no significant difference (ns).

3. Results and discussion

3.1. Preparation and characterization of MPNs-based nanovaccines

First of all, 8 arms PEG with N-hydroxysuccinimide esters (8aPEG) was chemically modified to engineer terminal-functionalized PEG polyphenols, including 8 arms PEG terminated with mannose and dopamine (Man-8aPEG-DA) and 8 arms PEG with dopamine terminals (8aPEG-DA), as building blocks of MPNs, and their chemical structures were verified by the ^{1}H NMR and UV–vis spectra. As shown in Fig. S1, characteristic peaks of dopamine at the chemical shifts of 6.42, 6.57, and 6.63 ppm confirmed that dopamine was successfully grafted on Man-8aPEG-DA and 8aPEG-DA. The peaks located from 4.3 ppm to 5.4 ppm, which could be attributed to the hydrogens of mannose, demonstrated mannose was connected to Man-8aPEG-DA. Based on the peak area integration and calculation, on average, 0.6 mannose as well as 6.2 dopamine molecules were grafted on each Man-8aPEG-DA macromolecule, and 7.7 dopamine molecules were decorated on each 8aPEG-DA macromolecule. Besides, the absorption peak at 280 nm in the UV–vis spectra also proved the existence of dopamine in Man-8aPEG-DA and 8aPEG-DA (Fig. S2).

Subsequently, PEG polyphenols and Fe^{3+} self-assembled into MPNs nanoparticles through the coordination between phenolic hydroxyl and Fe^{3+}, during which period model antigen ovalbumin (OVA) and immune adjuvant CpG could be concurrently encapsulated. The nanovaccines thus prepared contained mannose-decorated MPNs nanoparticles carrying OVA and CpG (MMOC), mannose-modified MPNs nanoparticles just loaded with OVA (MMO), and MPNs nanoparticles loaded with OVA and CpG but without the mannose decoration (MOC). The morphology and size distribution of nanovaccines were well investigated by transmission electron microscopy (TEM) and dynamic light scattering (DLS). As shown in Fig. 1a and Fig. S3, the nanovaccines exhibited a loose structure and particle size of about 40 nm. Whereas the average hydrodynamic sizes of MOC, MMO, and MMOC were 104.8 ± 3.0, 137.3 ± 0.9, and 142.5 ± 1.1 nm (Fig. 1b), respectively, which were larger than the particle sizes in TEM images. It was because the MPNs nanoparticles tended to relax and keep an extended state in solutions, thus displaying larger hydrodynamic sizes. The nanovaccines had narrow polydispersity indexes (PDI) (Fig. 1c) and negative zeta potentials (Fig. 1d), indicating their favorable dispersion and uniformity. The stability of MMOC was further assessed. After MMOC was incubated in the phosphate buffer solution (PBS) and fetal bovine serum (FBS) for 5 days, it showed good stability without significant change in the particle size (Fig. 1e). The addition of ethylene diamine tetraacetic acid (EDTA) caused the MMOC solution to fade in color, that is MMOC disintegrated, indicating that MPNs was formed through the coordination rather than other interactions (Fig. S4).

The loading of OVA and CpG was qualitatively and quantitatively investigated. As shown in Fig. 1f, the characteristic peaks at 1645 and 1524 cm^{-1}, which belonged to OVA, demonstrated that OVA was definitely encapsulated into MOC, MMO, and MMOC. Bradford protein assay kit and fluorescence spectrophotometer were severally used to ascertain the loading amounts of OVA and Cy5-labelled CpG. According to the standard curves (Fig. S5), 281.4 μg OVA and 56.2 μg CpG were loaded in MOC, 181.2 μg OVA was loaded in MMO, and 198.2 μg OVA

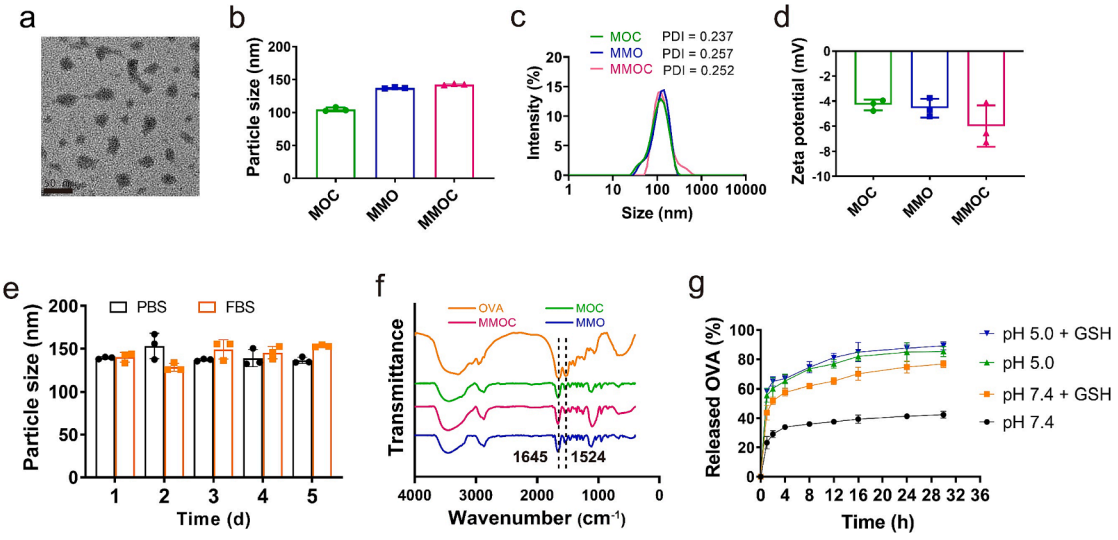

Fig. 1. Preparation and characterization of MPNs-based nanovaccines. a) TEM image of MMOC. b) Average hydrodynamic particle sizes, c) size distributions, and d) zeta potentials of MOC, MMO, and MMOC. e) The particle size change of MMOC incubated in the phosphate buffer solution (PBS) and fetal bovine serum (FBS). f) FT-IR spectra of OVA, MOC, MMO, and MMOC. g) Release behaviors of OVA from MMOC in different buffer solutions.

and 39.6 μg CpG were loaded in MMOC. The encapsulation efficiencies of OVA in MOC, MMO, and MMOC were 70.4 %, 45.3 %, and 49.6 %, respectively. The mannose decoration caused that the quantity of dopamine molecules in Man-8aPEG-DA was less than that in 8aPEG-DA. As a result, 8aPEG-DA was easier to assemble into MOC and encapsulated more OVA, while Man-8aPEG-DA with less dopamine was more difficult to form MMO and MMOC and loaded with less OVA. Fluorescence analysis indicated that the encapsulation efficiency of CpG in both MOC and MMOC was 100 %. The OVA release behavior in different circumstances was examined to evaluate the ability of MMOC to release antigen in a controlled manner. After MMOC was maintained under pH 5.0 and pH 7.4 with glutathione (GSH) for 1 h, the percentages of released OVA reached 55.5 % and 43.8 %, respectively (Fig. 1g). For comparison, only 23.2 % of OVA was released in the pH 7.4 group. At the timepoint of 30 h, released OVA in the groups of pH 7.4, pH 7.4 with GSH, and pH 5.0 severally accounted for 42.3 %, 76.8 %, and 85.3 %. Additionally, in the presence of both pH 5.0 and GSH, OVA more quickly dissociated from MMOC. These results revealed that MMOC possessed acidity and GSH sensitivities. In the condition of pH 5.0, phenolic hydroxyl anions could recover to phenolic hydroxyl, which greatly weakened the coordination ability of phenolic hydroxyl groups and broke the structure of MPNs. Moreover, GSH could competitively chelate to Fe^{3+}, leading to the rupture of coordinate bond between Fe^{3+} and phenolic hydroxyl anions. Therefore, both acidity and GSH could cause the disassembly of MPNs and promote the antigen release. Given the acidic lysosome and GSH-plentiful cytoplasm, MMOC was rationally anticipated to achieve the intelligent intracellular delivery of antigens.

3.2. *In vitro evaluations of cytotoxicity, antigen uptake, and intracellular co-localization*

Prior to various cellular assays, we assessed the cytotoxicity of nanovaccines fabricated in this study. After DC2.4 cells were treated with MOC, MMO, and MMOC for 24 h, the cell viability was determined by the CCK-8 assay. As shown in Fig. 2a, a distinct decrease of cell viability in every group could not be observed until the concentration arrived at 250 μg/mL. Even up to the high concentration of 500 μg/mL, cell viabilities in the groups of MOC, MMO, and MMOC, remained to be 73.3 %, 76.0 %, and 83.2 %, respectively. There was no significant hemolysis when the concentration of MMOC was between 31.3 μg/mL and 125 μg/mL (Fig. 2b and Fig. S6). The hemolysis rate at the concentration of 500 μg/mL was only 4.8 %. This result was well in agreement with the CCK-8 assay, showing the extremely low cytotoxicity of nanovaccines. It could owe the good biocompatibility to the harmfulless components of nanovaccines, such as PEG, Fe^{3+}, dopamine, OVA, and CpG. Afterwards, the intracellular antigen delivery efficiency of nanovaccines was evaluated. It has been widely reported that nanocarriers can improve the antigen uptake of APCs availably by the targeted delivery, increased recognition, and charge interaction. Accordingly, DC2.4 cells were used to evaluate the antigen endocytosis efficiency under the delivery function of MPNs nanovaccines. It can be seen that the mean fluorescence intensities (MFI) of OVA-FITC in the groups of MOC, MMO, and MMOC were obviously higher than that in the free OVA group (Fig. 2c), which indicated MPNs nanoparticles effectively promoted the OVA ingestion by DC2.4 cells through increasing the recognition size. Especially, MMOC exhibited the highest intracellular antigen delivery efficiency due to the mannose and mannose receptor-mediated endocytosis, which was confirmed by flow cytometry results (Fig. 2d and Fig. S7). Furthermore, the confocal laser scanning microscopy (CLSM) was employed to visually explore the intracellular location of OVA-FITC and CpG-Cy5 (Fig. 2e). Strong green and red fluorescence signals could be observed in the images of the MMOC group, demonstrating that MMOC indeed concurrently delivered both OVA and CpG into the same cell in an efficient way.

3.3. *In vitro antigen lysosome escape, cross-presentation, and BMDCs activation*

The critical point of exogeneous antigen inducing a mighty cellular immunity is that the antigen escapes from the siege of lysosome, so that exogeneous antigen can be processed by proteasome and further presented to T cells in the MHC I pathway. In consequence, we assessed the effect of nanovaccines on causing the antigen lysosome escape. As shown in Fig. 2f, lots of green fluorescence signals were external to the red fluorescence signals in the MMO and MMOC groups, indicating that MMO and MMOC effectively accelerated the separation of OVA from lysosomes and increased the efficiency of lysosomal escape. The phenolic group anions in MPNs nanoparticles could absorb hydrogen ions to restore to neutral phenolic groups, which imparted a buffering ability to MPNs nanoparticles so as to facilitate the rupture of lysosome via the proton sponge effect [53] and lead to the escape of OVA into cytoplasm. As a comparison, it revealed fewer green signals in the MOC group, which resulted from the low uptake of DC2.4 cells on MOC. The dual expressions of CD80 and CD86 can be viewed as the sign of DCs maturation. The proportion of CD80 and CD86 double positives in the MMOC group reached 44.2 %, which was significantly higher than those in the other groups (Fig. 2g and Fig. S8). It was precisely because MMOC delivered more OVA and CpG into BMDCs, and consequently BMDCs were greatly stimulated. The higher intracellular OVA accumulation, caused by MMOC, also motivated the highest MHC II expression on BMDCs among various groups (Fig. 2h and Fig. S9). In agreement with the result of antigen lysosome escape assay, both MMO and MMOC notably promoted the antigen cross-presentation efficiency. As such, OVA was processed into antigen peptide (SIINFEKL) and then presented in the MHC I route, which was verified by detecting the expression of SIINFEKL-H-2Kb. The proportions of SIINFEKL-H-2 Kb positive in the MMO and MMOC groups were 5.9 % and 6.1 %, respectively, with being significantly higher than those in the other groups (Fig. 2i and Fig. S10). Moreover, the measurement of proinflammation cytokines, containing IL-6, IL-12, TNF-α, and IFN-γ, secreted by BMDCs also demonstrated that MMOC effectively advanced the BMDCs activation and would probably elicit noticeable cellular immune responses (Fig. 2j-m). Due to the mannose-mediated endocytosis, MMOC could deliver more OVA and CpG into BMDCs than MOC. More intracellular OVA and CpG could largely motivate BMDCs and promote the MHC I antigen presentation. Accordingly, MMOC induced BMDCs to secrete higher cytokine levels than MOC.

3.4. *Antigen accumulation and DCs activation in lymph nodes*

Once the nanovaccine is captured by DCs, DCs will carry antigen to homing back to lymph nodes and initiate a cascade of following immune responses. Hence, the *in vivo* fluorescence imaging was conducted to study the arrival of OVA marked with Cy7 to lymph nodes (Fig. 3a). Although the signal of OVA-Cy7 at the inguinal lymph node in the OVA group could be found at 8 h, it disappeared at 24 and 48 h, implying the rapid clearance of body on free OVA. In contrast, there was still a strong fluorescence signal around the position of inguinal lymph node at 48 h in the MMOC group, which was derived from the efficient uptake of MMOC by DCs through the mannose-mediated endocytosis. To visibly display the distribution of OVA-FITC and CpG-Cy5 in the lymph node, inguinal lymph nodes were collected post vaccination, sliced, and observed using a confocal microscope. In Fig. 3b, it shows weak signals of OVA-FITC (green) and CpG-Cy5 (red) in the OVA + CpG and MOC groups, while the strong green signal of OVA-FITC could be seen in the MMO and MMOC groups. Moreover, a distinct red fluorescence signal of CpG-Cy5 also appeared in the MMOC group, demonstrating MMOC notably promoted the synchronous accumulation of OVA and CpG in the lymph node. The quantitative analysis was further carried out to ascertain the number of OVA in the lymph node. Fig. 3c reveals that the amounts of OVA in the inguinal lymph nodes of OVA, MOC, and MMOC

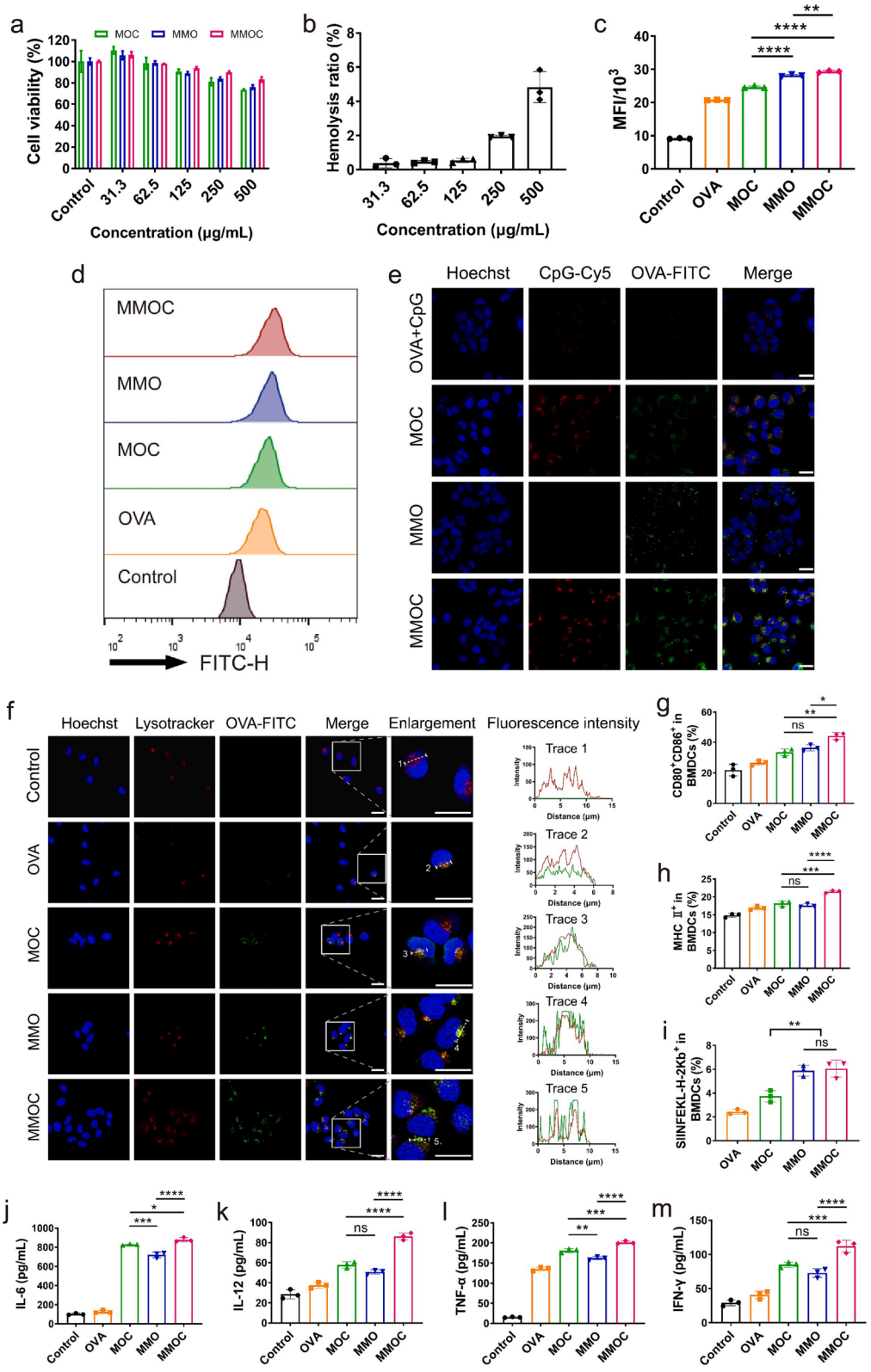

Fig. 2. In vitro cellular assays. a) Cell viability of DC2.4 cells treated by MOC, MMO, and MMOC. b) Hemolysis assessment on MMOC. c) Mean fluorescence intensity (MFI) and d) flow cytometry plots of DC2.4 cells incubated with various OVA-FITC-based vaccine formulations. e) Confocal laser scanning microscopy (CLSM) images for intracellular co-localization of OVA-FITC (green) and CpG-Cy5 (red). Scale bar represents 20 μm. f) CLSM images for the analysis of antigen lysosome escape effect. Scale bar represents 20 μm. The expressions of g) CD80 and CD86, h) MHC II, and i) SIINFEKL-H-2Kb on BMDCs treated with different vaccine formulations (gated on $CD11c^{+}$ DCs). The cytokine levels of j) IL-6, k) IL-12, l) TNF-α, and m) IFN-γ secreted by BMDCs. *$p < 0.05$, **$p < 0.01$, ***$p < 0.001$, and ****$p < 0.0001$. The ns means not significant.

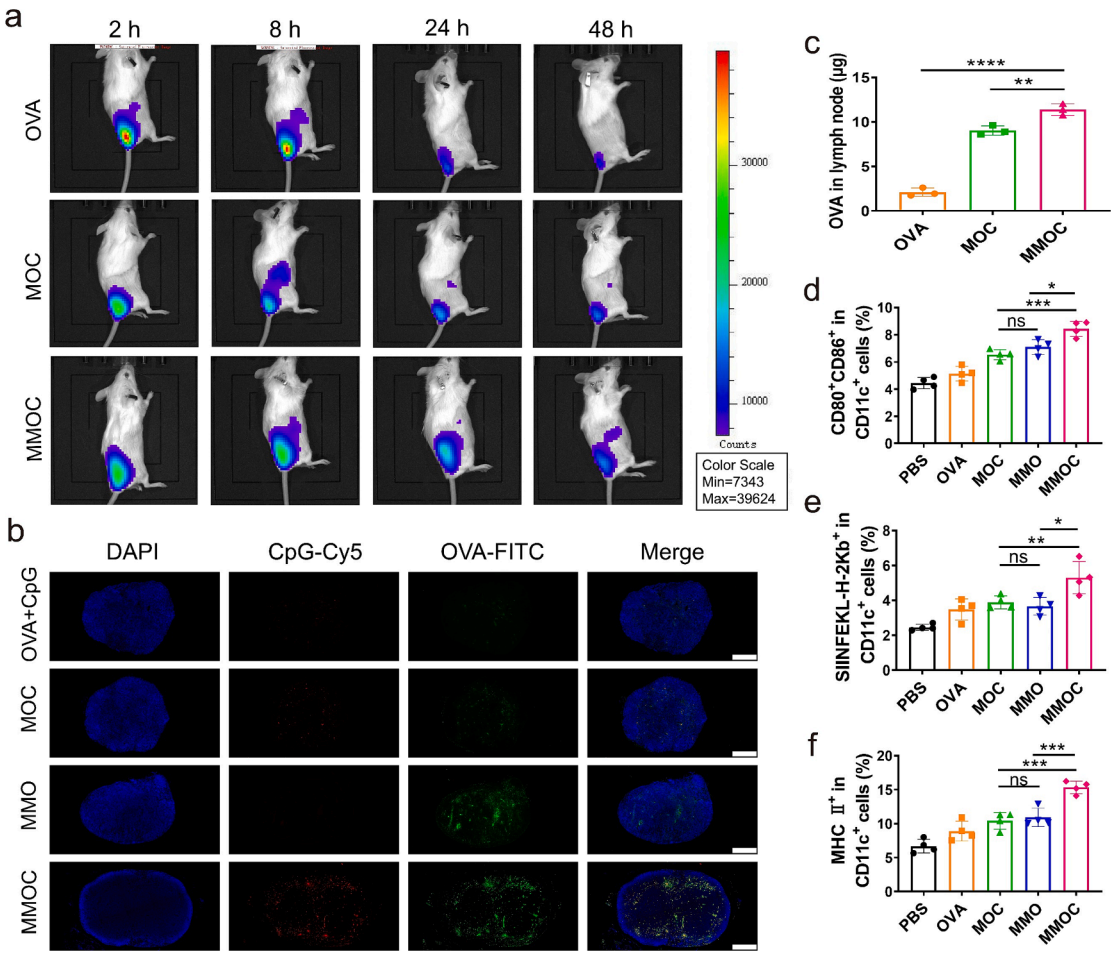

Fig. 3. Evaluations of antigen accumulation and DCs activation in lymph nodes. a) *In vivo* fluorescence imaging at different times after mice were subcutaneously injected with OVA, MOC, and MMOC at the tail base. OVA was labelled with Cy7. b) Distribution of OVA-FITC and CpG-Cy5 in the slices of inguinal lymph nodes that were collected at 24 h after mice were injected with various vaccine formulations. Cell nuclei were stained with DAPI. Scale bar is 400 μm. c) The quantities of OVA-FITC in lymph nodes after mice were injected with various vaccine formulations. The expressions of d) CD80 and CD86, e) SIINFEKL-H-2Kb, and f) MHC II on DCs harvested from the mice that were immunized with different vaccine formulations (gated on $CD11c^+$ cells). *p < 0.05, **p < 0.01, ***p < 0.001, and ****p < 0.0001. The ns means not significant.

groups were 2.1, 9.0, and 11.4 μg, respectively, which was consistent with the results of above imaging assays. In addition, the activation of DCs in lymph nodes was investigated. The highest dual-expression of CD80 and CD86 on $CD11c^+$ cells in the MMOC group indicated that MMOC greatly excited DCs (Fig. 3d). Besides, MMOC simultaneously enhanced the MHC I and MHC II presentations of OVA (Fig. 3e,f). These results demonstrated that MMOC was efficiently captured by DCs via the mannose-mediated endocytosis and then significantly excited DCs, which would conduce to eliciting a strong immune response.

3.5. *In vivo immune responses and biocompatibility*

As shown in Fig. 4a, after C57BL/6 mice were immunized with various vaccine formulations 3 times, splenocytes were harvested to investigate the T cell response. Given that $CD4^+$ T cells play an important role in regulating adaptive immunity and $CD8^+$ T cells are the main effector T cells during the cellular immune response, we measured the proliferation situation of $CD4^+$ and $CD8^+$ T cells in spleens. The frequencies of $CD4^+$ and $CD8^+$ T cells in the MMOC group were 17.1 % and 28.2 %, respectively, which were significantly higher than those in the other groups, indicating that MMOC induced a strong T cell-mediated adaptive immunity (Fig. 4b-e). Remarkably, the proportion of SIINFEKL-H-2Kb tetramer$^+$$CD8^+$ T cells in the MMOC group presented a 2.5-fold increase when compared with that in the OVA group (Fig. 4f and Fig. S11). It revealed that MMOC provoked a significant antigen-specific $CD8^+$ T cell proliferation, which could be attributed to the enhanced MHC I-involved cross-presentation triggered by MMOC. Because CTLs are the main force that directly destroys tumor cells, the CTLs response was further evaluated. After splenocytes were re-stimulated by OVA, the frequencies of $CD107a^+CD8^+$ and IFN-γ^+CD8^+ T cells in the MMOC group were 1.8- and 3.0-fold higher than those in the OVA group, respectively (Fig. 4g,h and Fig. S12-13). It demonstrated MMOC induced a potent antigen-specific CTLs response that would effectively depress the tumor growth. The cytokine levels of TNF-α, IFN-γ, IL-12, and IL-6 in the MMOC group were significantly higher than those in the other groups, which also proved MMOC elicited a Th1-inclined cellular immunity (Fig. 4i-l). Moreover, the essential function of cancer vaccine is to build an immune memory barrier that can timely attack the neogenetic tumor cell carrying the same antigen. Especially, the effector memory T cell that can react quickly upon encountering the same antigen is an important part of the immune memory system. Compared with other vaccine formulations, MMOC activated more $CD4^+$ and $CD8^+$ effector memory T (T_{EM}) cells, indicating that MMOC has established a reliable immune memory effect (Fig. 4m,n and Fig. S14).

In addition, the biological safety of nanovaccines was assessed. Main organs, including heart, liver, spleen, lung, and kidney, and sera were collected from C57BL/6 mice vaccinated with various vaccine

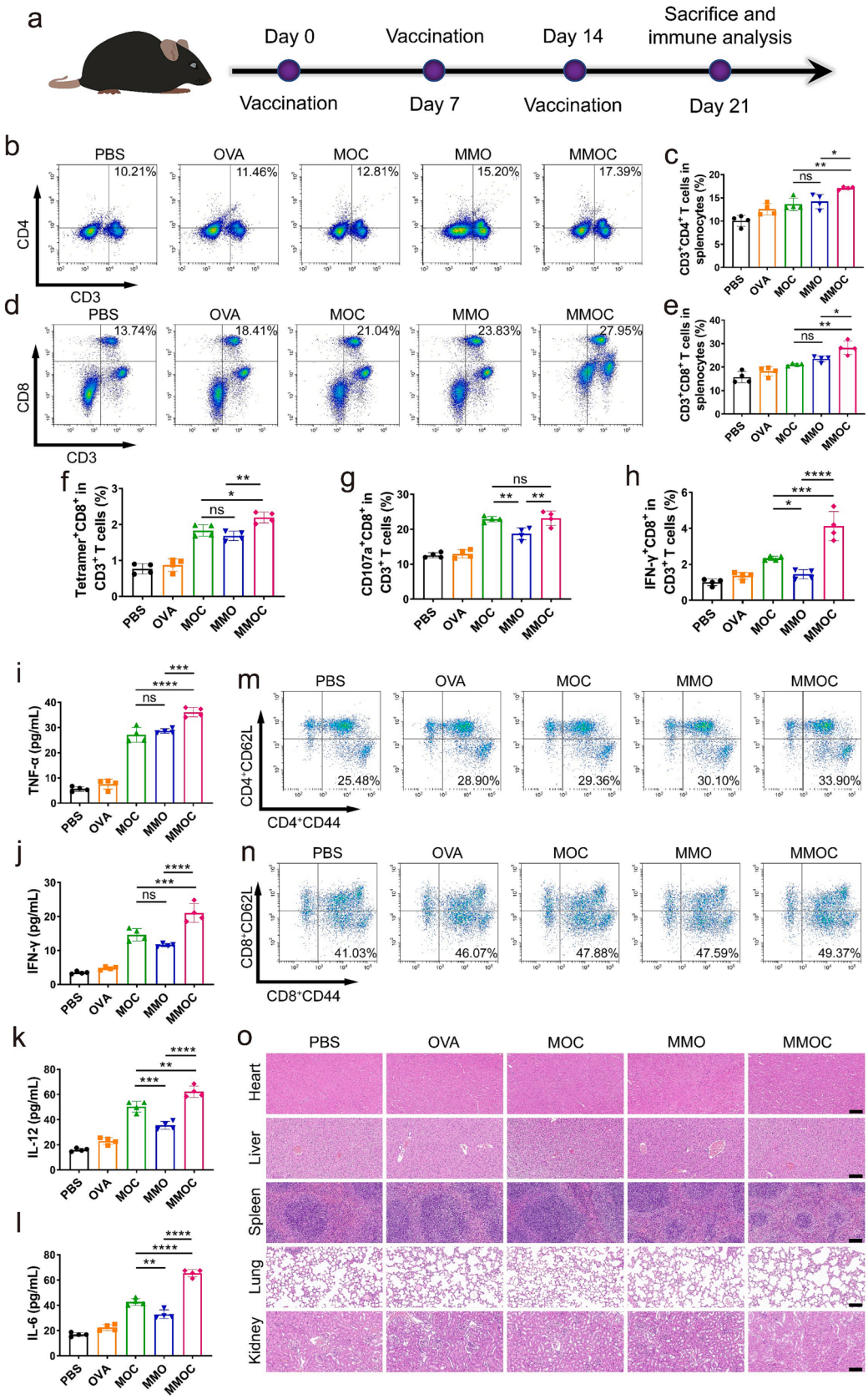

(caption on next page)

Fig. 4. *In vivo* immune responses and biocompatibility (n = 4). a) Schematic illustration for the immunization assay. b) Flow cytometry plots and c) analysis of $CD3^+CD4^+$ T cells in various groups (gated on splenocytes). d) Flow cytometry plots and e) analysis of $CD3^+CD8^+$ T cells in various groups (gated on splenocytes). The proportions of f) SIINFEKL-H-2Kb tetramer$^+CD8^+$, g) $CD107a^+CD8^+$, and h) IFN-γ^+CD8^+ T cells in spleens (gated on $CD3^+$ T cells). The cytokine levels of i) TNF-α, j) IFN-γ, k) IL-12, and l) IL-6 in sera. Flow cytometry plots of m) $CD4^+$ effector memory T cells (gated on $CD4^+$ cells) and n) $CD8^+$ effector memory T cells (gated on $CD8^+$ cells) in spleens. o) H&E images of main organs (heart, liver, spleen, lung, and kidney) harvested from the mice immunized with various vaccine formulations. Scale bar represents 100 μm. *$p < 0.05$, **$p < 0.01$, ***$p < 0.001$, and ****$p < 0.0001$. The ns means not significant.

formulations three times. Compared with the control group, MOC, MMO, and MMOC did not cause distinguishable histopathological abnormalities based on the H&E section analysis (Fig. 4o). The main biochemical indexes in sera of various groups were basically at normal levels (Fig. S15). These results demonstrated that the nanovaccines prepared in this study had an excellent biocompatibility *in vivo*.

3.6. Therapeutic and prophylactic effects on E.G7-OVA tumors

Encouraged by the notable MMOC-instigated cellular immunity, the specific antitumor capacity of MMOC on the E.G7-OVA tumor was studied. As shown in Fig. 5a, C57BL/6 mice were inoculated with E.G7-OVA tumor cells, whereafter vaccinated with various vaccine formulations 2 times. Tumor sizes and body weights were measured every 2 days, and finally tumors were collected after mice were sacrificed on day 18. The suppression effect of MOC, MMO, and MMOC on tumors was obviously superior to PBS and OVA, leading to a slower growth of tumor volumes (Fig. 5b and Fig. S16). In the end of therapeutic trial, the average tumor volume in the MMOC group was the smallest among all groups, which could be ascribed to the mighty OVA-specific CTLs response motivated by MMOC. Correspondingly, the average tumor weight in the MMOC group also presented to be the smallest (Fig. 5c). Additionally, body weights of mice in each group showed minor changes and located within the normal range all the time (Fig. 5d). The photograph of tumors obtained from the mice of various groups reveals that tumors in the MMOC group had the smallest sizes (Fig. 5e), which was consistent with the results of tumor volume and tumor weight. Images of tumor slices stained with Ki67, TUNEL, CD4, CD8, and Foxp3 markers show that there was a weak tumor cell proliferation, a significant cell apoptosis, more infiltrating $CD4^+$ and $CD8^+$ T cells, and fewer regulatory T cells (Tregs) in the MMOC group (Fig. 5f). These results indicated MMOC markedly intensified the antitumor cellular immunity in the tumor sites, so as to bring about the death of tumor cells and inhibit the tumor development.

As shown in Fig. 5g, after C57BL/6 mice have been immunized with different vaccine formulations 3 times, they were inoculated with E.G7-OVA cells to investigate the prevention effect of nanovaccines on newly emerging tumors. Once the tumor volume arrived at 1500 mm^3, the mouse was euthanized. Strikingly, the tumor growth was greatly retarded by virtue of the vaccination of MOC, MMO, and MMOC (Fig. 5h). In particular, it should be noted that 3 mice in the MMOC group did not grow tumor all through the assay, confirming the admirable preventing ability of MMOC. The survival rate curves in Fig. 5i display that 2 mice in the PBS group died as early as day 20, while none of mice in the MMOC group met the death criteria until day 32. On day 46, survival percentages in the groups of PBS, OVA, MOC, and MMO were all 0, however, the livability of the MMOC group was maintained at 60 %. These results demonstrated MMOC could effectively avoid the formation of tumors by means of evoking tumor-specific immune memory responses. Body weights of mice in every group showed small fluctuations and were still in the normal range (Fig. 5j).

3.7. Therapeutic and prophylactic effects on 4T1 tumors

To investigate the versatility of MPNs-based nanovaccines, CCMPs originating from 4T1 cell membranes were used as antigens to fabricate 3 nanovaccines, including mannose-modified MPNs nanoparticles loaded with CCMPs and CpG (MMCC), mannose-modified MPNs nanoparticles just loaded with CCMPs (MMC), and MPNs nanoparticles carrying CCMPs and CpG but without the mannose decoration (MCC). Through the BCA protein measurement assay, loading quantities of CCMPs in MCC, MMC, and MMCC were 195.6, 163.2, and 170.3 μg, respectively, and corresponding encapsulation efficiencies were severally 48.9 %, 40.8 %, and 42.6 % (Fig. S17). Thus, the loading situation of CCMPs was similar to that of OVA, which exhibited the versatility of MPNs nanoparticles as antigen carriers. TEM image and DLS result show that MMCC had a small particle size and narrow size distribution (Fig. S18-19). The release profiles of CCMPs in different conditions were tested. As shown in Fig. S20, the presence of both pH 5.0 and GSH notably accelerated the release of CCMPs from MMCC, which could be ascribed to the dual sensitivities of MPNs. Accordingly, MMCC had the ability of controllably releasing CCMPs in the cytoplasm so as to increase the use efficiency of antigens.

After 4T1 tumor models were established, various administrations were carried out by complying with the schedule (Fig. 6a). Above results of immunization assays demonstrated that the nanovaccine prepared in this study could notably activate antigen-specific CTLs. But, PD-1 of CTLs that is usually viewed as a negative immunoregulatory molecule will bind to PD-L1 highly expressed on tumor cells, which disables CTLs to limit the effectiveness of tumor immunotherapy. Hence, the PD1 antibody (anti-PD1) was used to blockade the tumor immune escape pathway of PD1/PD-L1, so as to enhance the immunotherapy efficacy in combination with cancer nanovaccine. Compared with PBS and uncombined CCMPs, the engineered nanovaccines of MCC, MMC, and MMCC evidently inhibited the progression of tumors (Fig. 6b and Fig. S21). Rationally, the joint usage of anti-PD1 exerted additional therapeutic benefits on 4T1 tumors. Body weights of the mice in various groups fluctuated slightly (Fig. 6c). On day 22, the mice were sacrificed, and meanwhile spleens and tumors were collected for the immune analysis. $CD4^+$ (Fig. 6d,e) and $CD8^+$ (Fig. 6f,g) T cells were found to be highly present in the spleens of MMCC and MMCC + anti-PD1 groups, indicating MMCC stimulated strong helper and effector T cells responses in the tumor-bearing mice. In the meantime, the high proliferation of $CD4^+$ and $CD8^+$ T_{EM} cells, triggered by MMCC, would help to resist the tumor recurrence and metastasis (Fig. 6h,i and Fig. S22-23). It was worth noting that the frequencies of Tregs ($CD4^+CD25^+Foxp3^+$ cells) in the MMCC and MMCC + anti-PD1 groups were 18.3 % and 10.4 %, respectively, which were significantly lower than those in the PBS and CCMPs groups (Fig. 6j,k). It demonstrated that MMCC led to a weaker negative immune regulation while activating a stronger cellular immunity. The high frequencies of $CD80^+CD86^+$ DCs in the tumors of MMCC and MMCC + anti-PD1 groups revealed that the immune system was indeed primed in the tumor microenvironment (Fig. 6l,m). More tumor-infiltrating $CD4^+$ and $CD8^+$ T cells resulting from MMCC (Fig. 6n-q), in conjunction with the immune checkpoint blockade of anti-PD1, were bound to vastly destroy tumor cells. On the contrary, fewer Tregs were present in the tumors of MMCC + anti-PD1 group (Fig. 6r and Fig. S24), which signified the immune-activated state of tumor microenvironment and improved the immunotherapy performance.

Additionally, the prevention efficacy on 4T1 tumors was evaluated after the BALB/c mice were immunized with CCMPs-based nanovaccines 3 times (Fig. 7a). Fig. 7b reveals that the vaccination of MCC, MMC, and MMCC obviously postponed the development of 4T1 tumors. Particularly, the tumors in the MMCC group were all in a slow-growing condition. On day 42 post the 4T1 cells inoculation, survival rates in the groups of PBS, CCMPs, MCC, MMC, and MMCC were 0, 0, 0, 20 %, and

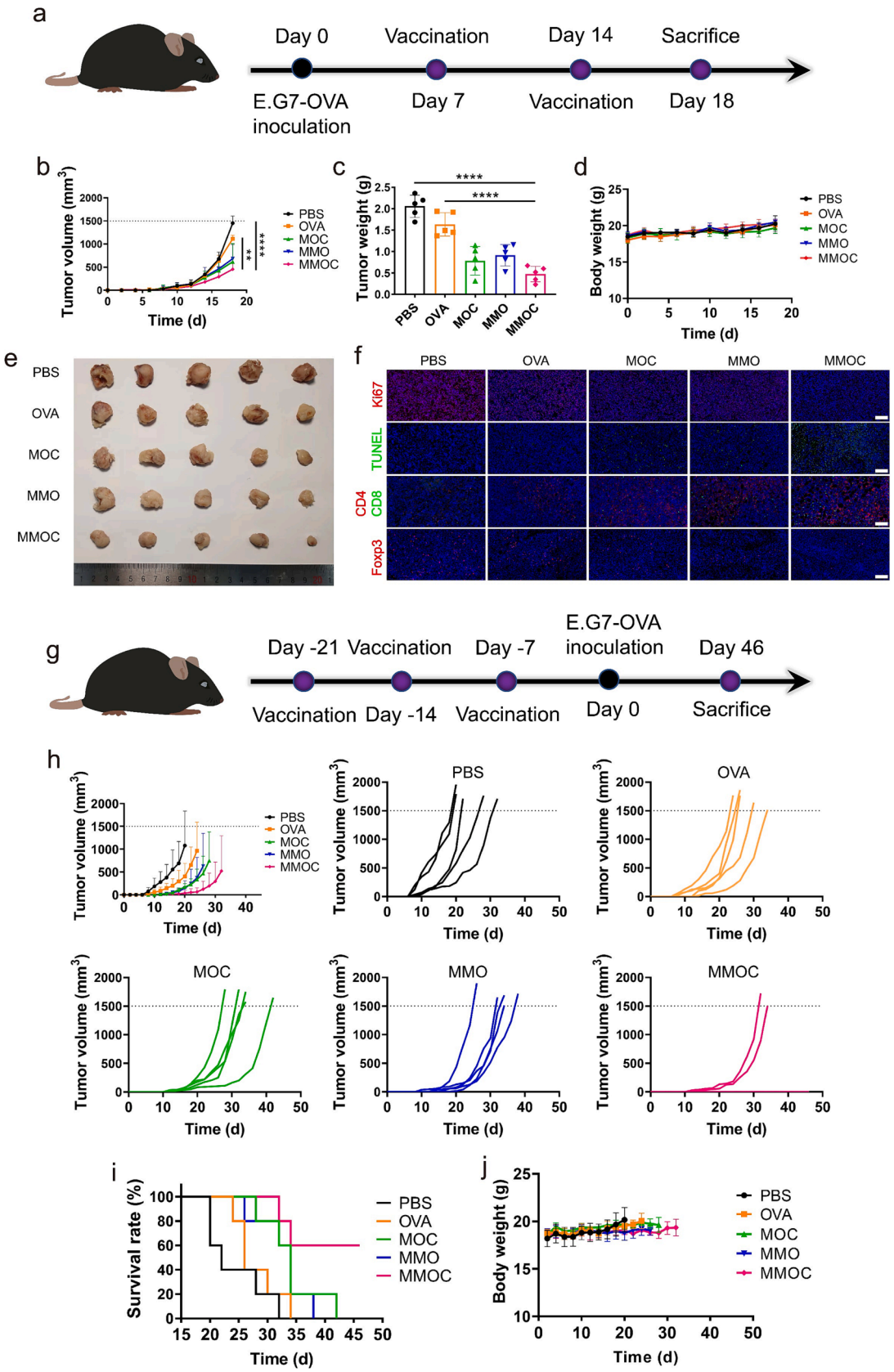

Fig. 5. *In vivo* antitumor challenge (n = 5). a) Schedule for the therapeutic trial on E.G7-OVA tumors. b) Tumor volume curves in different groups varying with time. c) Weights of tumors collected from the mice of various groups at the end of treatment. d) Body weights of mice varying with time. e) Photograph of tumors obtained from the mice in various groups at the end of treatment. f) Images of dissected tumors stained with Ki67, TUNEL, CD4, CD8, and Foxp3 markers. Scale bar represents 100 μm. g) Schedule for the preventive trial on E.G7-OVA tumors. h) Tumor volumes of mice in different groups varying with time. i) Survival rates of various groups varying with time. j) Body weights of mice varying with time. $^{**}p < 0.01$ and $^{****}p < 0.0001$.

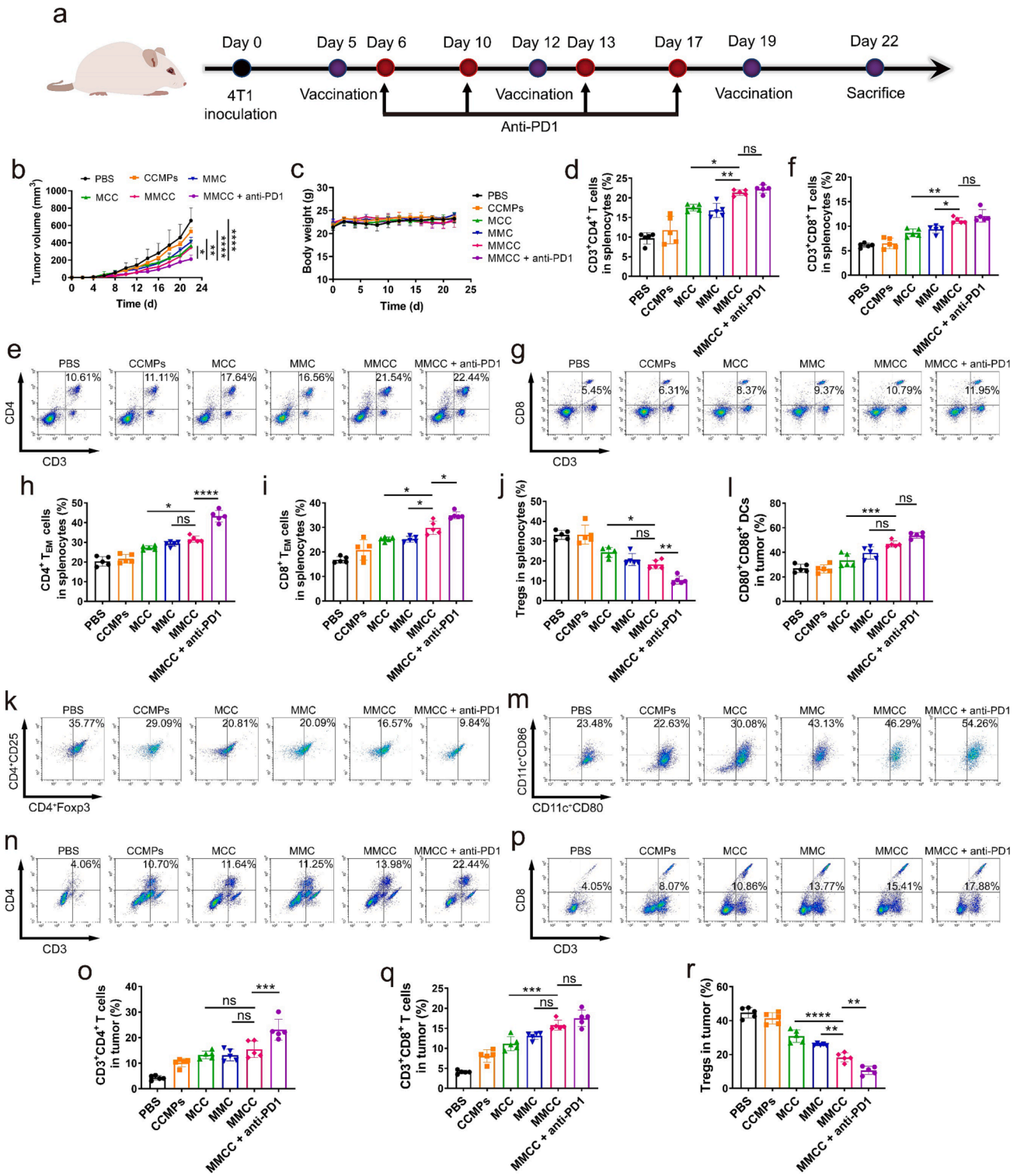

Fig. 6. *In vivo* treatment assessment on 4T1 tumors (n = 5). a) Schematic illustration for the therapeutic trial on 4T1 tumors. b) Tumor growth curves over time. c) Body weights of mice varying with time. d) Flow cytometry analysis and e) plots of $CD3^+CD4^+$ T cells in spleens (gated on splenocytes). f) Flow cytometry analysis and g) plots of $CD3^+CD8^+$ T cells in spleens (gated on splenocytes). Proportions of h) $CD4^+$ T_{EM} cells (gated on $CD4^+$ cells) and i) $CD8^+$ T_{EM} cells (gated on $CD8^+$ cells) in spleens. j) Frequencies and k) flow cytometry graphs of Tregs in spleens (gated on $CD4^+$ cells). l) Flow cytometry analysis and m) plots of $CD80^+CD86^+$ DCs in tumors (gated on $CD11c^+$ cells). n) Flow cytometry graphs and o) analysis of $CD3^+CD4^+$ T cells in tumors. p) Flow cytometry graphs and q) analysis of $CD3^+CD8^+$ T cells in tumors. r) Percentages of Tregs in tumors (gated on $CD4^+$ cells). *p < 0.05, **p < 0.01, ***p < 0.001, and ****p < 0.0001. The ns means not significant.

100 %, respectively (Fig. 7c). These results verified the splendid prevention capability of MMCC on 4T1 tumors. The vaccination of MMCC provoked a 4T1 tumor cell-specific immune response and memory effect by the targeted delivery of CCMPs to DCs, so that the mice could resist the occurrence of 4T1 tumors. Body weights in various groups scarcely changed over the 26 days (Fig. 7d), which revealed the excellent biosafety of MPNs nanovaccines. As shown in Fig. 7e, the proliferation activity of 4T1 tumor cells was dramatically depressed, and lots of $CD4^+$

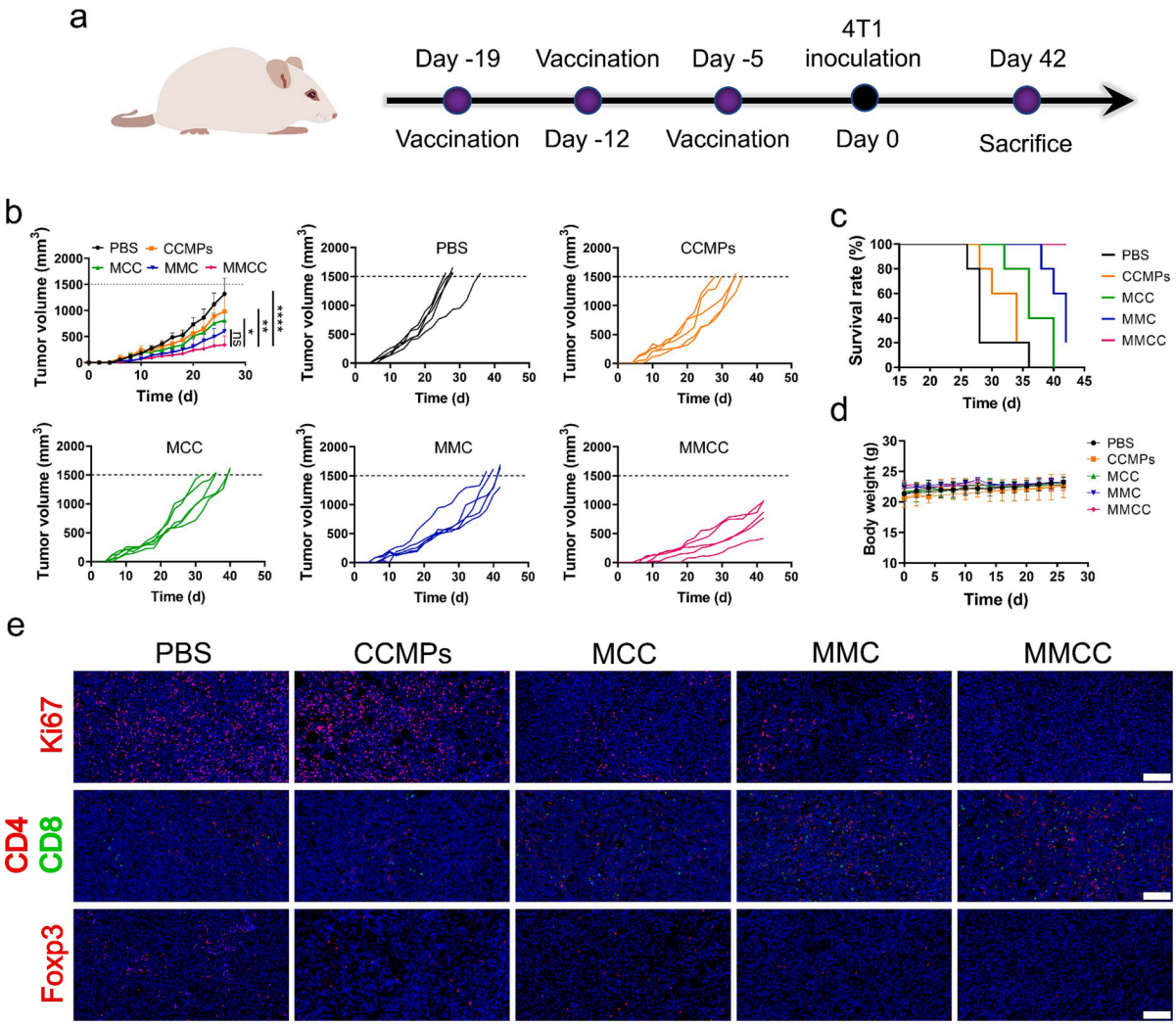

Fig. 7. *In vivo* prophylaxis assessment on 4T1 tumors (n = 5). a) Schematic illustration for the preventive trial on 4T1 tumors. b) Tumor growth curves after various treatments. c) Survival rates in different groups varying with time. d) Body weights of mice recorded 26 days after various treatments. e) Images of tumor tissues stained with Ki67, CD4, CD8, and Foxp3 markers. Scale bar represents 100 μm. *p < 0.05, **p < 0.01, and ****p < 0.0001. The ns means not significant.

and $CD8^+$ T cells and few Tregs infiltrated the tumor tissues in the MMCC group. It was precisely because MMCC induced an abundance of tumor-infiltrating $CD4^+$ and $CD8^+$ T cells that showed an effective killing effect on tumor cells, the growth of 4T1 tumors was greatly limited.

4. Conclusion

In this work, we propose a strategy for using MPNs nanoparticles as the antigen delivery platform to construct cancer nanovaccines. During the facile and rapid self-assembly of MPNs nanoparticles, antigen and CpG were simultaneously encapsulated. By taking advantage of the mannose-mediated endocytosis, the MMOC nanovaccine, carrying OVA and CpG, was efficiently ingested and notably activated BMDCs. The *in vivo* immunization assays show that MMOC had an excellent biocompatibility and could significantly evoke robust antigen-specific cellular immunity, the CTL response, and an immune memory effect. Therefore, MMOC performed a great efficacy in treating and preventing E.G7-OVA tumors. Furthermore, the all-purpose MPNs nanocarriers could also be loaded with 4T1 cell-derived CCMPs and CpG to prepare the MMCC nanovaccine. Therapeutic and prophylactic effects of MMCC on 4T1 tumors were also tested and the positive outcome of this strategy was demonstrated as well. Overall, MPNs-based cancer nanovaccines show a great versatility and potential for cancer immunotherapy and prevention.

CRediT authorship contribution statement

Xingyu Luo: Investigation, Project administration, Writing – original draft. **Xiaolu Chen:** Conceptualization, Data curation, Funding acquisition, Resources, Writing – original draft. **Rongying Ma:** Data curation, Investigation, Project administration. **Zhaoming Fu:** Investigation, Project administration. **Zuwei Liu:** Investigation, Methodology, Project administration. **Qianhong Su:** Investigation. **Huiling Fu:** Investigation. **Yong Yang:** Conceptualization, Formal analysis, Funding acquisition, Investigation, Methodology, Project administration, Resources, Supervision, Validation, Writing – review & editing. **Wei Xue:** Funding acquisition, Methodology, Resources, Supervision, Validation.

Declaration of competing interest

The authors declare that they have no known competing financial interests or personal relationships that could have appeared to influence the work reported in this paper.

Data availability

Data will be made available on request.

Acknowledgements

Xingyu Luo and Xiaolu Chen contributed equally to this work. This study was financially supported by the National Natural Science Foundation of China (32060225), Hainan Provincial Natural Science Foundation of China (520MS016), and Central Public-interest Scientific Institution Basal Research Fund for Chinese Academy of Tropical Agricultural Sciences (1630032022022).

Appendix A. Supplementary data

Supplementary data to this article can be found online at https://doi.org/10.1016/j.cej.2024.148611.

References

[1] A.D. Waldman, J.M. Fritz, M.J. Lenardo, A guide to cancer immunotherapy: from T cell basic science to clinical practice, Nat. Rev. Immunol. 20 (2020) 651–668.
[2] B.Q. Zhou, J.X. Liu, M.A. Lin, J.Y. Zhu, W.R. Chen, Recent advances in immunotherapy, immunoadjuvant, and nanomaterial-based combination immunotherapy, Coord. Chem. Rev. 442 (2021) 214009.
[3] J. Liu, M.Y. Fu, M.N. Wang, D.D. Wan, Y.Q. Wei, X.W. Wei, Cancer vaccines as promising immuno-therapeutics: platforms and current progress, J. Hematol. Oncol. 15 (2022) 28.
[4] G.N. Shi, C.N. Zhang, R. Xu, J.F. Niu, H.J. Song, X.Y. Zhang, W.W. Wang, Y. M. Wang, C. Li, X.Q. Wei, D.L. Kong, Enhanced antitumor immunity by targeting dendritic cells with tumor cell lysate-loaded chitosan nanoparticles vaccine, Biomaterials 113 (2017) 191–202.
[5] F.Y. Huang, S.Z. Dai, J.Y. Wang, Y.Y. Lin, C.C. Wang, W.P. Zheng, G.H. Tan, Engineered porous/hollow Burkholderia pseudomallei loading tumor lysate as a vaccine, Biomaterials 278 (2021) 121141.
[6] S.A.S. Najafabadi, A. Bolhassani, M.R. Aghasadeghi, Tumor cell-based vaccine: an effective strategy for eradication of cancer cells, Immunotherapy 14 (2022) 639–654.
[7] Z.L. Zeng, K.Y. Pu, Improving cancer immunotherapy by cell membrane-camouflaged nanoparticles, Adv. Funct. Mater. 30 (2020) 2004397.
[8] B. Liu, Y. Yang, Y. Chao, Z.S. Xiao, J.L. Xu, C.J. Wang, Z.L. Dong, L.Q. Hou, Q.F. Li, Z. Liu, Equipping cancer cell membrane vesicles with functional DNA as a targeted vaccine for cancer immunotherapy, Nano Lett. 21 (2021) 9410–9418.
[9] G.M. Piperno, F. Simoncello, O. Romano, S. Vodret, Y. Yanagihashi, R. Dress, C. A. Dutertre, M. Bugatti, P. Bourdeley, A. Del Prete, T. Schioppa, E.M.C. Mazza, L. Collavin, S. Zacchigna, R. Ostuni, P. Guermonprez, W. Vermi, F. Ginhoux, S. Bicciato, S. Nagata, N. Caronni, F. Benvenuti, TIM4 expression by dendritic cells mediates uptake of tumor-associated antigens and anti-tumor responses, Nat. Commun. 12 (2021) 2237.
[10] R. Smith, E.I. Wafa, S.M. Geary, K. Ebeid, S.O. Alhaj-Suliman, A.K. Salem, Cationic nanoparticles enhance T cell tumor infiltration and antitumor immune responses to a melanoma vaccine, Sci. Adv. 8 (2022) 3150.
[11] J. Schmidt, J. Chiffelle, M.A.S. Perez, M. Magnin, S. Bobisse, M. Arnaud, R. Genolet, J. Cesbron, D. Barras, B. Navarro Rodrigo, F. Benedetti, A. Michel, L. Queiroz, P. Baumgaertner, P. Guillaume, M. Hebeisen, O. Michielin, T. Nguyen-Ngoc, F. Huber, M. Irving, S. Tissot-Renaud, B.J. Stevenson, S. Rusakiewicz, D. Dangaj Laniti, M. Bassani-Sternberg, N. Rufer, D. Gfeller, L.E. Kandalaft, D. E. Speiser, V. Zoete, G. Coukos, A. Harari, Neoantigen-specific CD8 T cells with high structural avidity preferentially reside in and eliminate tumors, Nat. Commun. 14 (2023) 3188.
[12] T. Su, X. Liu, S.B. Lin, F.R. Cheng, G.Z. Zhu, Ionizable polymeric nanocarriers for the codelivery of bi-adjuvant and neoantigens in combination tumor immunotherapy, Bioact. Mater. 26 (2023) 169–180.
[13] L. Diao, M. Liu, Rethinking antigen source: cancer vaccines based on whole tumor cell/tissue lysate or whole tumor cell, Adv. Sci. 10 (2023) 230012.
[14] J. Xu, J. Lv, Q. Zhuang, Z.J. Yang, Z.Q. Cao, L.G. Xu, P. Pei, C.Y. Wang, H.F. Wu, Z. L. Dong, Y. Chao, C. Wang, K. Yang, R. Peng, Y.Y. Cheng, Z. Liu, A general strategy towards personalized nanovaccines based on fluoropolymers for post-surgical cancer immunotherapy, Nat. Nanotechnol. 15 (2020) 1043–1052.
[15] C.M. Le Gall, J. Weiden, L.J. Eggermont, C.G. Figdor, Dendritic cells in cancer immunotherapy, Nat. Mater. 17 (2018) 474–475.
[16] J.J. Baljon, J.T. Wilson, Bioinspired vaccines to enhance MHC class-I antigen cross-presentation, Curr. Opin. Immunol. 77 (2022) 102215.
[17] M.A. Swartz, J.A. Hubbell, S.T. Reddy, Lymphatic drainage function and its immunological implications: from dendritic cell homing to vaccine design, Semin. Immunol. 20 (2008) 147–156.
[18] Q.Q. Ni, F.W. Zhang, Y.J. Liu, Z.T. Wang, G.C. Yu, B. Liang, G. Niu, T. Su, G.Z. Zhu, G.M. Lu, L.J. Zhang, X.Y. Chen, A bi-adjuvant nanovaccine that potentiates immunogenicity of neoantigen for combination immunotherapy of colorectal cancer, Sci. Adv. 6 (2020) 6071.
[19] C. Xu, H. Hong, Y. Lee, K.S. Park, M.J. Sun, T.R. Wang, M.E. Aikins, Y. Xu, J. J. Moon, Efficient lymph node-targeted delivery of personalized cancer vaccines with reactive oxygen species-inducing reduced graphene oxide nanosheets, ACS Nano 14 (2020) 13268–13278.
[20] L. Ma, L. Diao, Z.F. Peng, Y. Jia, H.M. Xie, B.S. Li, J.T. Ma, M. Zhang, L.F. Cheng, D. W. Ding, X.O. Zhang, H.B. Chen, F.F. Mo, H. Jiang, G.Q. Xu, F.H. Meng, Z.Y. Zhong, M. Liu, Immunotherapy and prevention of cancer by nanovaccines loaded with whole-cell components of tumor tissues or cells, Adv. Mater. 33 (2021) 2104849.
[21] G.Z. Zhu, F.W. Zhang, Q.Q. Ni, G. Niu, X.Y. Chen, Efficient nanovaccine delivery in cancer immunotherapy, ACS Nano 11 (2017) 2387–2392.
[22] X.X. Xie, T. Song, Y. Feng, H.X. Zhang, G. Yang, C.H. Wu, F.M. You, Y.Y. Liu, H. Yang, Nanotechnology-based multifunctional vaccines for cancer immunotherapy, Chem. Eng. J. 437 (2022) 135505.
[23] L. Zhou, B. Hou, D.G. Wang, F. Sun, R.D. Song, Q. Shao, H. Wang, H.J. Yu, Y.P. Li, Engineering polymeric prodrug nanoplatform for vaccination immunotherapy of cancer, Nano Lett. 20 (2020) 4393–4402.
[24] M.M. Alam, C.M. Jarvis, R. Hincapie, C.S. McKay, J. Schimer, C.A. Sanhueza, K. Xu, R.C. Diehl, M.G. Finn, L.L. Kiessling, Glycan-modified virus-like particles evoke T helper type 1-like immune responses, ACS Nano 15 (2021) 309–321.
[25] D.W. Zhu, C.Y. Hu, F. Fan, Y. Qin, C.L. Huang, Z.M. Zhang, L. Lu, H. Wang, H. F. Sun, X.G. Leng, C. Wang, D.L. Kong, L.H. Zhang, Co-delivery of antigen and dual agonists by programmed mannose-targeted cationic lipid-hybrid polymersomes for enhanced vaccination, Biomaterials 206 (2019) 25–40.
[26] Y.Q. Du, T.T. Song, J. Wu, X.D. Gao, G.H. Ma, Y.C. Liu, Y.F. Xia, Engineering mannosylated pickering emulsions for the targeted delivery of multicomponent vaccines, Biomaterials 280 (2022) 121313.
[27] J. Chen, H.P. Fang, Y.Y. Hu, J.Y. Wu, S.J. Zhang, Y.J. Feng, L. Lin, H.Y. Tian, X. S. Chen, Combining mannose receptor mediated nanovaccines and gene regulated PD-L1 blockade for boosting cancer immunotherapy, Bioact. Mater. 7 (2022) 167–180.
[28] P.Y. Chou, S.Y. Lin, Y.N. Wu, C.Y. Shen, M.T. Sheu, H.O. Ho, Glycosylation of OVA antigen-loaded PLGA nanoparticles enhances DC-targeting for cancer vaccination, J. Control. Release 351 (2022) 970–988.
[29] X. Zhou, Q.H. Su, H.W. Zhao, X.Y. Cao, Y. Yang, W. Xue, Metal-phenolic network-encapsulated nanovaccine with pH and reduction dual responsiveness for enhanced cancer immunotherapy, Mol. Pharmaceut. 17 (2020) 4603–4615.
[30] Q. Li, Z.G. Teng, J. Tao, W.H. Shi, G.W. Yang, Y. Zhang, X.D. Su, L. Chen, W.J. Xiu, L.H. Yuwen, H. Dong, Y.B. Mou, Elastic nanovaccine enhances dendritic cell-mediated tumor immunotherapy, Small 18 (2022) 2201108.
[31] N.Q. Gong, Y.X. Zhang, X.C. Teng, Y.C. Wang, S.D. Huo, G.C. Qing, Q.K. Ni, X.L. Li, J.J. Wang, X.X. Ye, T.B. Zhang, S.Z. Chen, Y.J. Wang, J. Yu, P.C. Wang, Y.L. Gan, J. C. Zhang, M.J. Mitchell, J.H. Li, X.J. Liang, Proton-driven transformable nanovaccine for cancer immunotherapy, Nat. Nanotechnol. 15 (2020) 1053–1064.
[32] Y. Zhang, R.N. Sriramaneni, P.A. Clark, J.C. Jagodinsky, M.Z. Ye, W. Jin, Y. Y. Wang, A. Bates, C.P. Kerr, T. Le, R. Allawi, X.X. Wang, R.S. Xie, T.C. Havighurst, I. Chakravarty, A.L. Rakhmilevich, K.A. O'Leary, L.A. Schuler, P.M. Sondel, K. Kim, S.Q. Gong, Z.S. Morris, Multifunctional nanoparticle potentiates the in situ vaccination effect of radiation therapy and enhances response to immune checkpoint blockade, Nat. Commun. 13 (2022) 4948.
[33] R. Zhang, L. Tang, Y.S. Wang, Y.M. Tian, S.W. Wu, B.L. Zhou, C.Y. Dong, B.Y. Zhao, Y.L. Yang, D.Y. Xie, L. Yang, A dendrimer peptide (KK2DP7) delivery system with dual functions of lymph node targeting and immune adjuvants as a general strategy for cancer immunotherapy, Adv. Sci. 10 (2023) 2300116.
[34] M. Zhang, Y.M. Huang, J. Zou, Y. Yang, Y. Yao, G.F. Cheng, Y.N. Yang, Advanced oxidation nanoprocessing boosts immunogenicity of whole tumor cells, Adv. Sci. 10 (2023) 230225.
[35] X.K. Chen, Y. Zhang, Combination of tumor fragments and nanotechnology as a therapeutic approach: Treating a tumor with tumor, Nano Today 35 (2020) 100993.
[36] Z.Q. Meng, Y.J. Zhang, X.F. Zhou, J.S. Ji, Z. Liu, Nanovaccines with cell-derived components for cancer immunotherapy, Adv. Drug Deliv. Rev. 182 (2022) 114107.
[37] H. Ejima, J.J. Richardson, K. Liang, J.P. Best, M.P. van Koeverden, G.K. Such, J. W. Cui, F. Caruso, One-step assembly of coordination complexes for versatile film and particle engineering, Science 341 (2013) 154–157.
[38] H. Ejima, J.J. Richardson, F. Caruso, Metal-phenolic networks as a versatile platform to engineer nanomaterials and biointerfaces, Nano Today 12 (2017) 136–148.
[39] Q.G. Li, Z.L. Dong, M.W. Chen, L.Z. Feng, Phenolic molecules constructed nanomedicine for innovative cancer treatment, Coord. Chem. Rev. 439 (2021) 213912.
[40] Z.M. Fu, Y.F. Zhang, X.L. Chen, N. Wang, R.Y. Ma, X.Y. Luo, X. Pan, Y. Yang, W. Xue, A versatile nanoplatform based on metal-phenolic networks inhibiting tumor growth and metastasis by combined starvation/chemodynamic/immunotherapy, Adv. Funct. Mater. 33 (2023) 2211869.
[41] L.S. Xie, J. Li, L.Y. Wang, Y.L. Dai, Engineering metal-phenolic networks for enhancing cancer therapy by tumor microenvironment modulation, Wiley Interdiscip. Rev.: Nanomed. Nanobiotechnol. 15 (2023) e1864.
[42] Z.Q. Wang, Y.Q. Guo, Y. Fan, J.W. Chen, H. Wang, M.W. Shen, X.Y. Shi, Metal-phenolic-network-coated dendrimer-drug conjugates for tumor MR imaging and chemo/chemodynamic therapy via amplification of endoplasmic reticulum stress, Adv. Mater. 34 (2022) 2107009.
[43] X.L. Li, Z.Y. Duan, X.T. Chen, D.Y. Pan, Q. Luo, L. Gu, G. Xu, Y.G. Li, H. Zhang, Q. Y. Gong, R.J. Chen, Z.W. Gu, K. Luo, Impairing tumor metabolic plasticity via a stable metal-phenolic-based polymeric nanomedicine to suppress colorectal cancer, Adv. Mater. 35 (2023) 2300548.
[44] H. Tian, G.H. Wang, W. Sang, L.S. Xie, Z. Zhang, W.X. Li, J. Yan, Y. Tian, J. Li, B. Li, Y.L. Dai, Manganese-phenolic nanoadjuvant combines sonodynamic therapy with cGAS-STING activation for enhanced cancer immunotherapy, Nano Today 43 (2022) 101405.

[45] J.H. Han, H. Shin, J. Lee, J.M. Kang, J.H. Park, C.G. Park, D.K. Han, I.H. Kim, W. Park, Combination of metal-phenolic network-based immunoactive nanoparticles and bipolar irreversible electroporation for effective cancer immunotherapy, Small 18 (2022) 2200316.
[46] J. Yan, G.H. Wang, L.S. Xie, H. Tian, J. Li, B. Li, W. Sang, W.X. Li, Z. Zhang, Y. L. Dai, Engineering radiosensitizer-based metal-phenolic networks potentiate STING pathway activation for advanced radiotherapy, Adv. Mater. 34 (2022) 2105783.
[47] J. Li, L.S. Xie, W. Sang, W.X. Li, G.H. Wang, J. Yan, Z. Zhang, H. Tian, Q.L. Fan, Y. L. Dai, A metal-phenolic nanosensitizer performs hydrogen sulfide-reprogrammed oxygen metabolism for cancer radiotherapy intensification and immunogenicity, Angew. Chem., Int. Ed. 61 (2022) e202200830.
[48] Y.B. Wang, C.N. Xu, M. Meng, L. Lin, Y.Y. Hu, K. Hao, S. Sheng, S.J. Zhang, J. Y. Wu, F. Liu, X.E. Jiang, H.Y. Tian, X.S. Chen, Precise regulation of inflammation and immunosuppressive microenvironment for amplified photothermal/ immunotherapy against tumour recurrence and metastasis, Nano Today 40 (2021) 101266.
[49] D.D. Hu, H.X. Xu, W. Zhang, X.D. Xu, B. Xiao, X.Y. Shi, Z.X. Zhou, N.K.H. Slater, Y. Q. Shen, J.B. Tang, Vanadyl nanocomplexes enhance photothermia-induced cancer immunotherapy to inhibit tumor metastasis and recurrence, Biomaterials 277 (2021) 121130.
[50] X.L. He, H.F. Zhu, J.J. Shang, M.F. Li, Y.Y. Zhang, S.C. Zhou, G.D. Gong, Y.X. He, A. Blocki, J.L. Guo, Intratumoral synthesis of transformable metal-phenolic nanoaggregates with enhanced tumor penetration and retention for photothermal immunotherapy, Theranostics 12 (2022) 6258–6272.
[51] Q. Wang, Z.L. Gao, K.J. Zhao, P.Y. Zhang, Q.Z. Zhong, Q. Yu, S.M. Zhai, J.W. Cui, Co-delivery of enzymes and photosensitizers via metal-phenolic network capsules for enhanced photodynamic therapy, Chin. Chem. Lett. 33 (2022) 1917–1922.
[52] Q.H. Su, Z.W. Liu, R.L. Du, X.L. Chen, L.L. Chen, Z.M. Fu, X.Y. Luo, Y. Yang, X. Q. Shi, Facile preparation of a metal-phenolic network-based lymph node targeting nanovaccine for antitumor immunotherapy, Acta Biomater. 158 (2023) 510–524.
[53] J.Q. Chen, J.H. Li, J.J. Zhou, Z.X. Lin, F. Cavalieri, E. Czuba-Wojnilowicz, Y.J. Hu, A. Glab, Y. Ju, J.J. Richardson, F. Caruso, Metal-phenolic coatings as a platform to trigger endosomal escape of nanoparticles, ACS Nano 13 (2019) 11653–11664.